

# Theoretical and numerical modeling of shape memory alloys accounting for multiple phase transformations and martensite reorientation

F. Auricchio<sup>a</sup>, E. Bonetti<sup>b</sup>, G. Scalet<sup>c,\*</sup>, F. Ubertini<sup>c</sup>

<sup>a</sup>*Dipartimento di Ingegneria Civile e Architettura, Università di Pavia,  
Via Ferrata 3, 27100 Pavia, Italy*

<sup>b</sup>*Dipartimento di Matematica, Università di Pavia,  
Via Ferrata 1, 27100 Pavia, Italy*

<sup>c</sup>*Dipartimento di Ingegneria Civile, Chimica, Ambientale e dei Materiali, Università di Bologna,  
Viale Risorgimento 2, 40136 Bologna, Italy*

---

## Abstract

The present paper develops a refined and general three-dimensional phenomenological constitutive model for shape memory alloys (SMAs), along the lines of what recently proposed by Auricchio and Bonetti (2013) in a more theoretical context. Such an improved model takes into account several physical phenomena, as martensite reorientation and different kinetics between forward/reverse phase transformations, including also smooth thermo-mechanical response, low-stress phase transformations as well as transformation-dependent elastic properties. The model is treated numerically through an effective and efficient procedure, consisting in the replacement of the classical set of Kuhn-Tucker inequality conditions by the so-called Fischer-Burmeister complementarity function. Numerical predictions are compared with experimental results and the finite element analysis of a SMA-based real device is described to assess the reliability of the proposed model as well as the effectiveness of its numerical counterpart.

*Keywords:* Shape memory alloys, Constitutive modeling, Phase transformation, Reorientation, Fischer-Burmeister function

---

## 1. INTRODUCTION

Smart materials exhibit special properties that make them an attractive choice for industrial applications in many branches of engineering. Among different types of smart materials, shape memory alloys (SMAs) have unique features known as pseudo-elasticity (PE), one-way and two-way shape memory effects (SMEs) (Duerig et al., 1990; Otsuka and Wayman, 1998). Such unusual effects are exploited in a large variety of interesting applications. The most successful commercial

---

\*Corresponding author. DICAM, Università di Bologna, Viale Risorgimento 2, 40136 Bologna, Italy.  
Tel.: +39 051 2093374.

*Email address:* giulia.scalet2@unibo.it (G. Scalet)

examples are in the biomedical area, e.g., endo-prosthesis, orthodontic archwires, cardiovascular stents (Auricchio et al., 2010a; Azaouzi et al., 2013; Wu et al., 2007), as well as in the robotic and automotive areas, e.g., positioning for mirror seats, actuators, micro-grippers (Auricchio et al., 2009a, 2010b; Huang, 1998; Williams and Elahina, 2008).

SMA features are the consequence of reversible martensitic phase transformations (PTs) between a high symmetric austenitic phase and a low symmetric martensitic phase. Austenite is a solid phase, present at high temperature, which transforms into different possible martensitic variants by means of a lattice shearing mechanism. In thermal-induced transformations under zero stress, multi-direction martensite variants compensate each other and arrange themselves in a self accommodating manner through twinning, with no observable macroscopic shape change. In stress-induced transformations, starting from a martensitic specimen, the application of a loading induces a detwinning process of the martensitic variants, leading to the presence of a single-variant (Duerig et al., 1990); upon unloading, a large residual strain remains, which can be recovered by heating. This phenomenon is referred to as SME. On the other hand, when a stress is applied to an austenitic specimen, at high temperature, a transformation from austenite to single-variant martensite occurs; upon unloading, the strain attained during loading is recovered. This process is referred to as PE (Otsuka and Wayman, 1998).

Such functional material properties motivate researchers to formulate constitutive models able to catch the interesting behavior of SMAs and to develop robust computational tools for practical purposes. In the following, we focus on both the constitutive and numerical modeling of SMAs by briefly reviewing some approaches available from the literature and by carefully describing our motivations and proposed improvements.

### *1.1. CONSTITUTIVE MODELING: STATE OF ART AND PROPOSED IMPROVEMENTS*

In the past three decades SMAs have been deeply investigated from the point of view of modeling, analysis, and computation with the focus on a variety of aspects, such as, for instance, stress- and temperature-induced transformations, martensite reorientation or cyclic effects.

In terms of modeling, there have been several attempts to properly reproduce SMA material features. The resulting models can be categorized as either micro, micro-macro or macro. For an overview, see (Khandelwal and Buravalla, 2009; Lagoudas et al., 2006; Patoor et al., 2006).

In the following, we focus on phenomenological macro-modeling approaches which appear to be a powerful tool for the direct simulation of SMA applications, thanks to their simple numerical implementation and reduced time-consuming calculations, compared to micro-mechanical approaches. In particular, the present research is devoted to the aim of finding a flexible and accurate three-dimensional phenomenological model for a reliable description of SMA-based real devices behavior.

In the phenomenological framework, an appropriate set of internal variables has to be chosen to represent at least a scalar and a directional information (Luig and Bruhns, 2008). Physical motivations usually lead to the introduction of a martensite volume fraction and of a tensorial variable describing martensitic inelastic deformation processes (Arghavani et al., 2010; Luig and Bruhns, 2008; Peultier et al., 2006; Saleeb et al., 2011). Such a simplified description is motivated by the aim to obtain fast and efficient models with a low number of fitting parameters.

A set of only scalar variables is, in fact, not adequate due to the loss of explicit directional information. For instance, the model by Frémond (2002) describes SMA behavior in terms of austenite and two martensite variants and assumes the transformation strain direction to be known, although experimental studies showed that variant reorientation can be considered as a main phenomenon in SMA non-proportional loadings (Bouvet et al., 2002; Grabe and Bruhns, 2009; Helm and Haupt, 2003; Lim and McDowell, 1999; Sittner et al., 1995; Sun and Li, 2002).

On the other hand, models with only tensorial internal variables, by explicitly including simple directional information, seem to be more successful, but present some limitations since scalar and directional informations are tightly interconnected, possibly leading to limited or constrained modeling approaches. As an example, the model by Souza et al. (1998), then investigated by (Auricchio and Petrini, 2004a,b), introduces the transformation strain tensor as an internal variable and presents a simple and robust algorithm, widely used for implementation within finite element (FE) codes. On the contrary, it is not able to capture PTs for low levels of stress, as required often by industrial applications (Auricchio et al., 2009a), and does not include some secondary effects that may turn out to be relevant in practical cases (Thamburaja and Anand, 2001).

Numerous analyses of existing models and their comparison to experimental results have shown that current SMA constitutive models have reached a high level of sophistication. Several authors extended, in fact, such simplified phenomenological descriptions by using additional variables as volume fraction of twinned/detwinned martensites (Lexcelent et al., 2000; Panico and Brinson, 2007; Popov and Lagoudas, 2007), twins accommodation strain (Chemisky et al., 2011), viscoplasticity (Chemisky et al., 2014), thermo-mechanical coupling (Morin et al., 2011a,b; Zaki and Moumni, 2007a,b) or plastic strain (Auricchio et al., 2007; Hartl et al., 2010; Peng et al., 2012; Saint-Sulpice et al., 2009; Zaki et al., 2010). The recent and innovative work by Sedláč et al. (2012) formulates a new dissipation function to simulate non-proportional loadings and includes anisotropic behavior of textured SMAs as well as the thermo-mechanical response due to austenite-R-phase transformation. Panoskaltis et al. (2004) developed a three-dimensional thermo-mechanical constitutive model based on generalized plasticity theory in the small deformation regime, and Panoskaltis et al. (2011a,b) within finite strains and rotations.

However, the most capable models usually achieve accuracy at the cost of complexity, since they consider multiple and simultaneous processes (Chemisky et al., 2011; Popov and Lagoudas, 2007) or require costly calibrations of a high number of model parameters (Saleeb et al., 2013b, 2011).

Starting from the reviewed literature about constitutive modeling, the present paper is motivated by the necessity of developing constitutive models that can predict the complex thermo-mechanical behavior of SMAs and that can also be implemented numerically. Such models have to accurately capture material response not only during classical PE and SME loading paths, but also during loading paths involving the co-existence of all the three material phases, i.e., austenite, multiple- and single-variant martensite. Moreover, model material parameters have to be derived from a simple physical interpretation, which is important for the calibration process, to allow a quantitative validation through experimental results.

Indeed, the goal of the present paper is to introduce a refined, flexible and general three-dimensional phenomenological constitutive model for SMAs, along the lines of the recent theoretical work by Auricchio and Bonetti (2013), limiting the discussion to the small deformation regime.

The model by Auricchio and Bonetti (2013) addresses a general flexible theoretical framework for the development of constitutive models able to describe multiple phase transformations (PTs), which may or may not interact. The model is investigated from a purely mathematical point of view, by proposing some general considerations on requirements to be satisfied to make the model thermo-dynamically consistent. In particular, the cited reference does not cover several fundamental details, i.e., constitutive modeling detailing to SMAs, model parameters' physical interpretation and identification, as well as numerical modeling.

As concerns the constitutive modeling, the cited work gives only some very general indications on the effective modeling of SMA materials and, as a matter of fact, it reports only a very simple one-dimensional qualitative hand-computed response of the model. In fact, the cited reference does not apply in details the model to the case of SMAs and, at the same time, it does not give any indication on the possibility of effectively and robustly solving the complex set of possible PTs occurring in real SMAs, which represents the essential starting point into SMA modeling.

As concerns the model parameters' physical interpretation and identification, the cited reference does not address the important issue related to the physical interpretation of model parameters, as a clear and effective parameter identification procedure is an important key for the employment of a constitutive model by engineers in real-life simulations. In particular, model parameters are defined as general constants or general functions of temperature and volume fractions.

Finally, as concerns the numerical modeling, the cited model does not address any numerical solution algorithm to model formulation, which is important for engineers needing to perform accurate simulations for the design and study of the response of SMA structures or components.

In this context, the present paper aims to do a step-forward with respect to the work by Auricchio and Bonetti (2013) by deepening all the listed lacking aspects and to possibly offer a new contribution to the existing modeling solutions. The purpose is to formulate a general, complete and flexible theoretical framework that can predict the complex behavior of SMAs and is based on a physical interpretation of material parameters as well as to offer a robust numerical framework to be then used for the simulation of real devices.

From the modeling point of view, the proposed model combines the main features of the approaches by Frémond (2002) and Souza et al. (1998) and describes secondary effects in PTs as well as directional information for the transformation strain. Volume proportions of different configurations of crystal lattice (i.e., austenite, single- and multiple-variant martensites) are used as scalar internal variables and the direction of single-variant martensite as tensorial internal variable. With respect to the model by Frémond (2002), the present model considers the transformation strain direction unknown, by assuming the direction of single-variant martensite as tensorial internal variable. Compared to the model by Souza et al. (1998), the proposed theoretical framework allows for a completely independent description of the different PTs, leading to a very flexible frame in terms of model features and allowing to capture PTs at low levels of stress. As an example, Section 4.1 presents a detailed description of the one-dimensional stress-temperature phase diagram related to the proposed model and a comparison with that related to the model by Souza et al. (1998).

Compared to the model by Auricchio and Bonetti (2013), the proposed model naturally presents similarities in terms of theoretical aspects and governing equations. In the present work, however, we propose an enriched generalization, able to describe several phenomena such as martensite

reorientation, different kinetics between forward/reverse phase transformations, smooth thermo-mechanical response, low stress phase transformations, transformation-dependent elastic properties. In particular, the characteristics that have been included and improved upon in this work concern the asymmetric behavior between forward and reverse phase transformations, hardening effects, increasing hysteresis width for low applied stresses in thermal-cycling tests at constant load, the width of the hysteresis loop in superelasticity (i.e., difference between upper and lower plateau stress) decreasing with increasing temperature, smooth thermo-mechanical response, transformation dependent elastic properties. As an example, in order to include the listed characteristics in the theoretical model and to reproduce experimental evidences, we assign a significant flexibility to the model in terms of ability by introducing very special forms for the elastic domain radii.

We remark, moreover, that the proposed modeling approach presents similarities with some three-dimensional phenomenological models presented in the literature, in terms of capturing the reorientation process in martensite. Among others, we can cite the interesting works by Arghavani et al. (2010) and Chemisky et al. (2011). The model by Arghavani et al. (2010) describes the evolution of transformation strain with a unique martensitic volume fraction and considers a proportional relationship between the evolution of transformation strain and the evolution of the martensitic volume fraction; the model by Chemisky et al. (2011) adds to the classical internal variables, representing the martensite volume fraction and the mean transformation strain of martensite, two new variables accounting for the strain mechanism related to the accommodation of twins and for the self-accommodated martensite volume fraction. The final model is able to describe martensitic transformation and reorientation, and the inelastic accommodation of twins in self-accommodated martensite, as well as to account for tension-compression asymmetry and internal loops. Compared to the cited references, the proposed approach is very flexible since it can capture loading paths involving the co-existence of three material phases.

From the physical point of view, material parameters are then derived from a simple physical interpretation, and thus, are no more represented as general constants or general functions of temperature and volume fractions.

In the following Section, the proposed improvements in terms of numerical aspects are treated in detail.

## *1.2. NUMERICAL MODELING: STATE OF ART AND PROPOSED IMPROVEMENTS*

The present work focuses on another important aspect of SMA modeling, i.e., the development of an appropriate model implementation into numerical softwares (such as FE packages) to guarantee a robust computational tool, which could be effectively utilized for practical purposes. From a numerical point of view, robust and efficient integration algorithms for the zero-dimensional problem (e.g., constitutive equations at the Gauss point level in a FE scheme) need to be proposed in order to then solve complex boundary-value problems and to simulate SMA real devices behavior within FE codes. Some examples of SMA models are available in the literature in a suitable form to conduct three-dimensional thermo-mechanical simulations (Arghavani et al., 2011; Auricchio and Petrini, 2004a; Gao et al., 2007; Hartl et al., 2009, 2010; Helm, 2007; Lagoudas et al., 2012; Peultier et al., 2008; Popov and Lagoudas, 2007; Sedlák et al., 2012; Stupkiewicz and Petryk, 2012; Zaki, 2012a,b).

Generally, SMA macroscopic models are solved by return-map algorithms, either through norm regularization schemes at the cost of inaccuracy due to the corresponding approximation (Auricchio and Petrini, 2004a,b; Auricchio and Stefanelli, 2004) or nucleation-completion conditions (Arghavani et al., 2011). The recent work by Sedláč et al. (2012) applies the Nelder-Mead minimization algorithm to solve the derived energy minimization problem and introduces a regularization energy to assure the fulfillment of constraints on internal variables. Stupkiewicz and Petryk (2012) presented a pseudoelastic model within the incremental energy minimization framework and proposed an unified augmented Lagrangian treatment of both constitutive constraints and non-smooth dissipation function. The recent works by Peigney and Seguin (2013); Peigney et al. (2011) propose a new numerical approach for a micro-mechanical material model, based on the reformulation of the incremental problem as a linear complementarity problem (LCP), which can be solved using well established algorithms such as interior-point methods. Solving the obtained LCP allows to fully take the constraints on the internal variable into account and leads to an efficient numerical algorithm. The work by Popov and Lagoudas (2007) applies an extension of the closest point projection algorithm to describe a SMA model incorporating single- and multi-variant martensites. The work by Hartl et al. (2009) proposes a three-dimensional constitutive model capturing conventional SMA functional properties and thermal strain recovery, and additionally considering the initiation and evolution of plastic strains. The model is numerically implemented in a FE framework using a return mapping algorithm to solve the constitutive equations at each material point. The model is tested for three-dimensional FE analyses of SMA structural components under uniaxial and bending loads and then compared to experimental results of a bending member, illustrating the predictive accuracy of the model and its implementation.

However, algorithm schemes still need robustness investigations, aiming also at the development of flexible, effective and efficient procedures, applicable to models as the one introduced in the present work. In fact, the numerical application of standard predictor-corrector methods is not suitable for the proposed approach, because an elaborate active set search has to be carried out. Compared to the work by Hartl et al. (2009), for instance, the model deals with multiple scalar and tensorial internal variables, whose evolution is strongly coupled, and involving several constitutive constraints imposed on internal variables, which introduce additional complexity in the incremental schemes used in FE computations and, consequently, decrease algorithmic efficiency.

For these reasons different approaches need to be explored for the proposed modeling framework to describe situations corresponding to nucleation, saturation or completion of transformation.

Recalling the discussion of Section 1.1, the model by Auricchio and Bonetti (2013) does not address any numerical solution algorithm to model formulation.

The purpose of the present paper to integrate the proposed constitutive equations is to reduce the complexity, and thus increase the efficiency, of the algorithmic treatment. This is achieved by eliminating the need for a predictor-corrector-type scheme and by automatically constraining the range of the variant volume fractions. Consequently, we conduct the numerical investigation of the proposed model through an effective and efficient procedure, introduced in the framework of crystal plasticity by Schmidt-Baldassari (2003). It consists in replacing the Kuhn-Tucker complementarity inequality conditions by the equivalent Fischer-Burmeister complementarity function (Fischer, 1992) and in making possible to omit an active set search, a fundamental advantage when

dealing with many coupled evolution equations.

Besides the contributions by Bartel and Hackl (2009, 2010); Bartel et al. (2011) in the context of SMA micro-mechanical modeling, the work by Kiefer et al. (2012) presents two alternative algorithms for the integration of the coupled, non-linear and inelastic constitutive equations for magnetic shape memory alloy, i.e., the classical predictor-corrector return-mapping scheme and the Fischer-Burmeister based algorithm. The work shows the greater numerical efficiency of the second algorithm that is however tested for simple loading cases and not for three-dimensional analyses.

The proposed paper presents a detailed investigation of the numerical Fischer-Burmeister based algorithm, applied to the case of SMAs, to test its robustness and efficiency. This is achieved through: (i) a complete presentation of the adopted algorithmic scheme; (ii) the description of possible computational difficulties and related solutions; (iii) several numerical simulations, ranging from simple uniaxial tests to more complex three-dimensional FE analyses of a real-life device; and (iv) details about CPU times, number of steps and iterations. Moreover, FE analyses allow to qualitatively show and emphasize all the model features, while the comparison between numerical predictions and experimental data allows to quantitatively validate the proposed model and to demonstrate its reliability.

The present paper is organized as follows. The proposed three-dimensional phenomenological model is presented in Section 2. Section 3 describes the numerical implementation of model equations and the full solution algorithm. Section 4 presents model phase diagram and calibration. Section 5 is devoted to numerical tests and comparisons with experimental results. Conclusions and summary are finally given in Section 6.

## 2. A 3-D PHENOMENOLOGICAL MODEL FOR SMAs

This Section initially addresses a general three-dimensional phenomenological model for SMAs along the lines of the recent theoretical work by Auricchio and Bonetti (2013) and then, it proposes a simplified formulation based on physically motivated considerations.

In the following, we adopt superscripts  $A$ ,  $M$ , and  $S$  to indicate austenite, multiple-variant and single-variant martensites, respectively. Moreover, we make use of the notation  $\|\cdot\|$  to denote the Euclidean norm and of  $|\cdot|$  to indicate the absolute value function. The notation  $(\cdot : \cdot)$  denotes the inner product between two second order tensors (Gurtin et al., 2010).

### 2.1. A GENERAL MODEL FORMULATION

In the framework of macroscopic modeling and of small strain continuum mechanics, we assume the total strain,  $\boldsymbol{\epsilon}$ , representing the total deformation of the material, and temperature,  $T$ , as state variables. A general assumption of additive strain decomposition is adopted in the form:

$$\boldsymbol{\epsilon} = \boldsymbol{\epsilon}^e + \boldsymbol{\epsilon}^{ie} + \boldsymbol{\epsilon}^{th} \quad (1)$$

where  $\boldsymbol{\epsilon}^e$ ,  $\boldsymbol{\epsilon}^{ie}$  and  $\boldsymbol{\epsilon}^{th}$  denote the elastic, inelastic and thermal strain, respectively. The inelastic strain,  $\boldsymbol{\epsilon}^{ie}$ , should include the description of several physical phenomena, ranging from permanent

plasticity and PTs, up to void generation and fracture. In the following, all inelastic phenomena are neglected except for reversible martensitic PTs which are considered in combination with martensite reorientation.

Recalling the discussion reported in Section 1, the model introduces scalar and tensorial internal variables taking into account different PTs between austenite, multiple- and single-variant martensites as well as directional information for the transformation strain. The model decouples the pure reorientation from the pure transformation mechanism, but additionally, takes into account for temperature-induced transformation. Consequently, similarly to (Arghavani et al., 2010; Chemisky et al., 2011), we do not treat the inelastic strain,  $\boldsymbol{\epsilon}^{ie}$ , as a unique tensor variable, but we clearly distinguish between its norm and direction with the aim of getting more modeling freedom. In the following, we choose a measure of the amount of single-variant martensite as scalar internal variable, being related to the amount of inelastic strain due to stress-induced PT, while the average direction of different variants (or preferred direction of variants) as tensorial internal variable, representing the inelastic strain direction. Consequently, we may clearly interpret these two internal variables as PT and variant reorientation in order to hopefully describe transformation and reorientation with more flexibility. Moreover, we choose a measure of the amount of multiple-variant martensite as scalar internal variable, being related to the amount of martensite due to thermal-induced PT.

According to the previous discussion, volume proportions of different configurations of crystal lattice (austenite and martensite variants) are assumed as scalar internal variables and are represented by three phase parameters,  $\chi^A$ ,  $\chi^M$ ,  $\chi^S$ , standing, respectively, for austenite, multiple-variant and single-variant martensite, such that  $\chi^A, \chi^M, \chi^S \in [0, 1]$  and  $\chi^A + \chi^M + \chi^S = 1$ . Thanks to this last constraint, the model restricts itself just to two independent phase variables,  $\chi^M$  and  $\chi^S$ , letting  $\chi^A = 1 - \chi^M - \chi^S$ . Then, the following restrictions need to be fulfilled:

$$0 \leq \chi^M, \chi^S \leq 1, \quad \chi^M + \chi^S \leq 1 \quad (2)$$

Consequently, the inelastic strain is given by:

$$\boldsymbol{\epsilon}^{ie} = \varepsilon_L \chi^S \mathbf{d}^{tr} \quad (3)$$

where  $\varepsilon_L$  is a material parameter related to the maximum transformation strain reached at the end of the transformation during an uniaxial test (Otsuka and Ren, 2005), while  $\mathbf{d}^{tr}$  is the direction of single-variant martensite, assumed as tensorial internal variable with the following constraint:

$$\|\mathbf{d}^{tr}\| = 1 \quad (4)$$

We remark, again, that the choice of dealing with a tensorial variable,  $\mathbf{d}^{tr}$ , and two scalar variables,  $\chi^M$  and  $\chi^S$ , allows to distinguish between a phase to which no macroscopic strain is associated and a phase to which a homogenized macroscopic strain is associated, as well as to consider thermal-induced transformations when no stress is applied. Moreover, the model is able to distinguish between the norm and the direction of the inelastic strain,  $\boldsymbol{\epsilon}^{ie}$ , similarly to other effective modeling approaches as the one proposed in Arghavani et al. (2010); Chemisky et al. (2011), but allowing to get a richer model compared, for instance, to the works by Auricchio and Petrini (2004a,b); Frémond (2002); Souza et al. (1998).

### 2.1.1. Helmholtz free-energy function

The Helmholtz free-energy function,  $\Psi = \Psi(\boldsymbol{\epsilon}, T, \chi^M, \chi^S, \mathbf{d}^{tr})$ , is assumed in the following form:

$$\Psi = \Psi^{el} + \Psi^{ch} + \Psi^{int} + \Psi^v \quad (5)$$

where  $\Psi^{el}$  is the elastic energy,  $\Psi^{ch}$  the chemical energy related to entropic changes due to PTs,  $\Psi^{int}$  the interaction or interfacial energy, often derived from micro-mechanical or metallurgical considerations (Chemisky et al., 2011; Moumni et al., 2008; Peultier et al., 2006), and  $\Psi^v$  the energy due to internal constraints.

For the first two components of the free-energy, i.e.,  $\Psi^{el} = \Psi^{el}(\boldsymbol{\epsilon}, \chi^M, \chi^S, \mathbf{d}^{tr})$  and  $\Psi^{ch} = \Psi^{ch}(T, \chi^M, \chi^S)$ , presented in Eq. (5), we employ the rule of mixtures (Lagoudas et al., 2006), considering that each of them is a combination of austenite, multiple-variant and single-variant martensites. In particular, we set:

$$\begin{cases} \Psi^{el} = (1 - \chi^M - \chi^S) \Psi^{el,A} + \chi^M \Psi^{el,M} + \chi^S \Psi^{el,S} \\ \Psi^{ch} = (1 - \chi^M - \chi^S) \Psi^{ch,A} + \chi^M \Psi^{ch,M} + \chi^S \Psi^{ch,S} \end{cases} \quad (6)$$

To treat the elastic energy of Eq. (6)<sub>1</sub>,  $\Psi^{el}$ , we develop the aspect of phase mixture following the model of Reuss, by assuming the material as elastically isotropic with a homogeneous distribution of stresses in austenite, multiple-variant and single-variant martensites. The elastic energy term,  $\Psi^{el}$ , follows:

$$\Psi^{el} = \frac{1}{2} K \theta^2 + G \|\mathbf{e} - \varepsilon_L \chi^S \mathbf{d}^{tr}\|^2 - 3\alpha K \theta (T - T_0) \quad (7)$$

where  $T_0$  is the equilibrium temperature;  $\theta = \text{tr}(\boldsymbol{\epsilon})$  and  $\mathbf{e}$  is the deviatoric part of the strain tensor,  $\boldsymbol{\epsilon}$ , such that  $\boldsymbol{\epsilon} = \mathbf{e} + 1/3\theta\mathbf{I}$ ,  $\mathbf{I}$  being the second-order identity tensor and  $\text{tr}(\cdot)$  the trace operator. The bulk modulus,  $K$ , is assumed equal for all phases and the total shear modulus,  $G = G(\chi^M, \chi^S)$ , is determined from the Reuss model (Wagner and Windl, 2008), i.e.:

$$\begin{cases} K = K^A = K^M = K^S \\ \frac{1}{G} = (1 - \chi^M - \chi^S) \frac{1}{G^A} + \chi^M \frac{1}{G^M} + \chi^S \frac{1}{G^S} \end{cases} \quad (8)$$

The last right-side term of Eq. (7) derives from the assumption that  $\boldsymbol{\epsilon}^{th} = \boldsymbol{\alpha}(T - T_0)$ ,  $\boldsymbol{\alpha} = \alpha\mathbf{I}$  being the thermal expansion coefficient tensor.

To treat the chemical energy of Eq. (6)<sub>2</sub>,  $\Psi^{ch}$ , we define the free-energies of pure phases at stress-free conditions,  $\Psi^{ch,i} = \Psi^{ch,i}(T)$ , as:

$$\Psi^{ch,i} = u_0^i - s_0^i T + c^i \left[ (T - T_0) - T \log \frac{T}{T_0} \right] \quad (9)$$

for  $i \in A, M, S$ . Here  $u_0^i$  and  $s_0^i$  are the internal energy and entropy of the  $i$ -phase at a fixed equilibrium temperature,  $T_0$ ;  $c^i$  is the constant heat capacity of the  $i$ -phase (Leclercq and LExcellent, 1996; LExcellent et al., 2006; Panico and Brinson, 2007).

The free-energy component,  $\Psi^{int} = \Psi^{int}(\chi^M, \chi^S)$ , presented in Eq. (5), represents the interactions that appear between the phases, typically the incompatibilities between deformations (Leclercq and LExcellent, 1996; Raniecki et al., 1992). One of the characteristics of this energy is that it must disappear when only one phase is present inside the material. Moreover, in the case of three phases coexisting, this term must take into account interactions between one phase and the two remaining ones, separately (one interface separates two phases and not three). Indeed, we assume the following expression for the configurational energy (this expression has the great advantage to become fairly simple):

$$\Psi^{int} = (1 - \chi^M - \chi^S) \left( \bar{\Psi}^{AM} \chi^M + \bar{\Psi}^{AS} \chi^S + \bar{\Psi}^{AMS} \chi^M \chi^S \right) + \bar{\Psi}^{MS} \chi^M \chi^S \quad (10)$$

$\bar{\Psi}^{AM}$ ,  $\bar{\Psi}^{AS}$ ,  $\bar{\Psi}^{MS}$ , and  $\bar{\Psi}^{AMS}$  being material constants indicating interaction energies between phases  $A$  and  $M$ ,  $A$  and  $S$ ,  $M$  and  $S$ ,  $A$ ,  $M$  and  $S$ , respectively (Leclercq and LExcellent, 1996; Raniecki et al., 1992).

To satisfy constraints (2) and (4) on internal variables, we define the free-energy contribution,  $\Psi^v$ , presented in Eq. (5), as:

$$\Psi^v = I_{[0,1]}(\chi^M, \chi^S) + I_1(\|\mathbf{d}^{tr}\|) \quad (11)$$

where the indicator function,  $I_{[0,1]}(\chi^M, \chi^S)$ , is set to enforce inequality constraints (2) on  $\chi^M$  and  $\chi^S$  as (Rockafellar, 1970):

$$I_{[0,1]}(\chi^M, \chi^S) = \begin{cases} 0 & \text{if } 0 \leq \chi^M, \chi^S \leq 1, \chi^M + \chi^S \leq 1 \\ +\infty & \text{otherwise} \end{cases} \quad (12)$$

and the indicator function,  $I_1(\|\mathbf{d}^{tr}\|)$ , is defined to enforce equality constraint (4) on  $\mathbf{d}^{tr}$  as:

$$I_1(\|\mathbf{d}^{tr}\|) = \begin{cases} 0 & \text{if } \|\mathbf{d}^{tr}\| = 1 \\ +\infty & \text{otherwise} \end{cases} \quad (13)$$

In conclusion, the energy term,  $\Psi$ , reads as:

$$\begin{aligned} \Psi = & \frac{1}{2} K \theta^2 + G \|\mathbf{e} - \varepsilon_L \chi^S \mathbf{d}^{tr}\|^2 - 3\alpha K \theta (T - T_0) \\ & + u_0^A - s_0^A T + c^A \left[ (T - T_0) - T \log \frac{T}{T_0} \right] \\ & - (\Delta u^{AM} \chi^M + \Delta u^{AS} \chi^S) + (\Delta s^{AM} \chi^M + \Delta s^{AS} \chi^S) T \\ & - (\Delta c^{AM} \chi^M + \Delta c^{AS} \chi^S) \left[ (T - T_0) - T \log \frac{T}{T_0} \right] \\ & + (1 - \chi^M - \chi^S) \left( \bar{\Psi}^{AM} \chi^M + \bar{\Psi}^{AS} \chi^S + \bar{\Psi}^{AMS} \chi^M \chi^S \right) \\ & + \bar{\Psi}^{MS} \chi^M \chi^S + I_{[0,1]}(\chi^M, \chi^S) + I_1(\|\mathbf{d}^{tr}\|) \end{aligned} \quad (14)$$

where:

$$\begin{cases} \Delta u^{AM} = u_0^A - u_0^M \\ \Delta u^{AS} = u_0^A - u_0^S \end{cases} \quad \begin{cases} \Delta s^{AM} = s_0^A - s_0^M \\ \Delta s^{AS} = s_0^A - s_0^S \end{cases} \quad \begin{cases} \Delta c^{AM} = c^A - c^M \\ \Delta c^{AS} = c^A - c^S \end{cases} \quad (15)$$

### 2.1.2. Constitutive equations

Starting from the adopted free-energy,  $\Psi$ , presented in Eq. (14), and following standard arguments (Gurtin et al., 2010), we derive the volumetric and the deviatoric part of the stress tensor,  $\boldsymbol{\sigma}$ , denoted, respectively, with  $p$  and  $\mathbf{s}$ , and the entropy,  $\eta$ :

$$\begin{cases} p = \frac{\partial \Psi}{\partial \theta} = K\theta - 3\alpha K(T - T_0) \\ \mathbf{s} = \frac{\partial \Psi}{\partial \mathbf{e}} = 2G(\mathbf{e} - \varepsilon_L \chi^S \mathbf{d}^{tr}) \\ \eta = -\frac{\partial \Psi}{\partial T} = s_0^A - (\Delta s^{AM} \chi^M + \Delta s^{AS} \chi^S) + (c^A - \Delta c^{AM} \chi^M - \Delta c^{AS} \chi^S) \log \frac{T}{T_0} + 3\alpha K\theta \end{cases} \quad (16)$$

as well as the thermodynamic forces,  $B^M$ ,  $B^S$  and  $\mathbf{B}^d$ , associated to  $\chi^M$ ,  $\chi^S$  and  $\mathbf{d}^{tr}$ , respectively:

$$\begin{cases} B^M = -\frac{\partial \Psi}{\partial \chi^M} = -\frac{\partial G}{\partial \chi^M} \|\mathbf{e} - \varepsilon_L \chi^S \mathbf{d}^{tr}\|^2 + \Delta u^{AM} - \Delta s^{AM} T + \Delta c^{AM} \left[ (T - T_0) - T \log \frac{T}{T_0} \right] \\ \quad - \left( \bar{\Psi}^{AM} + \bar{\Psi}^{AMS} \chi^S \right) (1 - 2\chi^M - \chi^S) + \left( \bar{\Psi}^{AS} - \bar{\Psi}^{MS} \right) \chi^S - \gamma^M \\ B^S = -\frac{\partial \Psi}{\partial \chi^S} = 2G\varepsilon_L (\mathbf{e} - \varepsilon_L \chi^S \mathbf{d}^{tr}) : \mathbf{d}^{tr} - \frac{\partial G}{\partial \chi^S} \|\mathbf{e} - \varepsilon_L \chi^S \mathbf{d}^{tr}\|^2 \\ \quad + \Delta u^{AS} - \Delta s^{AS} T + \Delta c^{AS} \left[ (T - T_0) - T \log \frac{T}{T_0} \right] \\ \quad - \left( \bar{\Psi}^{AM} + \bar{\Psi}^{AMS} \chi^M \right) (1 - \chi^M - 2\chi^S) + \left( \bar{\Psi}^{AS} - \bar{\Psi}^{MS} \right) \chi^M - \gamma^S \\ \mathbf{B}^d = -\frac{\partial \Psi}{\partial \mathbf{d}^{tr}} = 2G\varepsilon_L \chi^S (\mathbf{e} - \varepsilon_L \chi^S \mathbf{d}^{tr}) - \gamma^d \mathbf{d}^{tr} \end{cases} \quad (17)$$

Variables  $\gamma^M$  and  $\gamma^S$  are defined as:

$$\gamma^M = \partial I_{[0,1]}(\chi^M, \chi^S) = \begin{cases} \gamma^{M0} \leq 0 & \text{if } \chi^M = 0 \\ 0 & \text{if } 0 < \chi^M < 1 \\ \gamma^{MS} \geq 0 & \text{if } \chi^M + \chi^S = 1 \end{cases} \quad (18)$$

and

$$\gamma^S = \partial I_{[0,1]}(\chi^M, \chi^S) = \begin{cases} \gamma^{S0} \leq 0 & \text{if } \chi^S = 0 \\ 0 & \text{if } 0 < \chi^S < 1 \\ \gamma^{MS} \geq 0 & \text{if } \chi^M + \chi^S = 1 \end{cases} \quad (19)$$

while

$$\gamma^d = \partial I_1(\|\mathbf{d}^{tr}\|) \neq \emptyset \text{ if } \|\mathbf{d}^{tr}\| = 1 \quad (20)$$

We can rewrite Eqs. (18)-(19) in terms of the classical Kuhn-Tucker complementarity conditions:

$$\begin{cases} \chi^M \geq 0, \gamma^{M0} \leq 0, \gamma^{M0} \chi^M = 0 \\ \chi^S \geq 0, \gamma^{S0} \leq 0, \gamma^{S0} \chi^S = 0 \\ (\chi^M + \chi^S - 1) \leq 0, \gamma^{MS} \geq 0, \gamma^{MS} (\chi^M + \chi^S - 1) = 0 \end{cases} \quad (21)$$

Moreover, we may observe that, in the case of proportional loading, i.e., neglecting the re-orientation process, by definition, the preferred variant direction,  $\mathbf{d}^{tr}$ , coincides with the deviatoric stress direction,  $\mathbf{s}$ . Under this assumption, we may simplify model equations by setting  $\mathbf{d}^{tr} = \mathbf{s}/\|\mathbf{s}\|$ .

### 2.1.3. Evolution equations and limit functions

As traditionally done in the context of associative evolution, we assume the evolution equations of internal variables as follows:

$$\begin{cases} \dot{\chi}^M = \dot{\zeta}^M \frac{B^M}{|B^M|} \\ \dot{\chi}^S = \dot{\zeta}^S \frac{B^S}{|B^S|} \\ \dot{\mathbf{d}}^{tr} = \dot{\zeta}^d \frac{\mathbf{B}^d}{\|\mathbf{B}^d\|} \end{cases} \quad (22)$$

where  $\dot{\zeta}^M$ ,  $\dot{\zeta}^S$  and  $\dot{\zeta}^d$  are non-negative consistency parameters.

Then, we define three limit functions,  $F^M = F^M(B^M)$ ,  $F^S = F^S(B^S, \chi^S, T)$  and  $F^d = F^d(\mathbf{B}^d, \chi^S)$ , playing the role of yield functions (Lubliner, 1990), to describe PTs and reorientation evolutions, in the following form:

$$\begin{cases} F^M = |B^M| - R^M \\ F^S = |B^S| - R^S \\ F^d = \|\mathbf{B}^d\| - R^d \end{cases} \quad (23)$$

where  $R^M$  and  $R^S = R^S(B^S, \chi^S, T)$  represent the positive radii of elastic domains to activate temperature and pure transformations, respectively, while  $R^d = R^d(\chi^S)$  represents a positive threshold value for the component of stress in the direction normal to the preferred direction of variants to activate variant reorientation. We observe that the proposed limit functions depend on the three thermodynamic forces,  $B^M$ ,  $B^S$ , and  $\mathbf{B}^d$ , and on the radii,  $R^M$ ,  $R^S$ , and  $R^d$ , whose adopted forms determine the specific dependencies of each limit function.

The model is finally completed by the classical Kuhn-Tucker and consistency conditions, as follows:

$$\begin{cases} \dot{\zeta}^M \geq 0, F^M \leq 0, \dot{\zeta}^M F^M = 0, \dot{\zeta}^M \dot{F}^M = 0 \\ \dot{\zeta}^S \geq 0, F^S \leq 0, \dot{\zeta}^S F^S = 0, \dot{\zeta}^S \dot{F}^S = 0 \\ \dot{\zeta}^d \geq 0, F^d \leq 0, \dot{\zeta}^d F^d = 0, \dot{\zeta}^d \dot{F}^d = 0 \end{cases} \quad (24)$$

A significant flexibility is assigned to the model in terms of ability to reproduce experimental evidences by introducing a very special form for  $R^S$ . In particular, through a proper choice of  $R^S$  we can guarantee the following features:

- asymmetric behavior between forward and reverse PTs, also modeled, for instance, in the works by Bouvet et al. (2004); Lagoudas et al. (2012);

- hardening effects, also modeled, for instance, in the work by Bouvet et al. (2004);
- increasing hysteresis width for low applied stresses in thermal-cycling tests at constant load, as experimentally demonstrated by Shaw and Kyriakides (1995); Stachowiak and McCormick (1987, 1988) and also modeled, for instance, in the works by Brinson (1993); Chemisky et al. (2011); Lagoudas et al. (2012); Panico and Brinson (2007); Peultier et al. (2008); Popov and Lagoudas (2007);
- width of the hysteresis loop in superelasticity (i.e., difference between upper and lower plateau stress) decreasing with increasing temperature, as experimentally demonstrated by Sittner et al. (2009) and also modeled, for instance, in the work by Sedláč et al. (2012);
- smooth thermo-mechanical response, as experimentally demonstrated by Hartl et al. (2010); Lagoudas et al. (2006) and also modeled, for instance, in the work by Lagoudas et al. (1996).

To take into account all these aspects we introduce the following very specific form for  $R^S$ :

$$R^S = \begin{cases} R_{f0}^S + h_f^S \chi^S + a_{f0}^S (\chi^S)^n + a_{f1}^S (1 - \chi^S)^n & \text{if } B^S \geq 0 \\ R_{r0}^S - h_r^S \chi^S - c_T^S (T - T_0) + a_{r0}^S (\chi^S)^n + a_{r1}^S (1 - \chi^S)^n & \text{if } B^S < 0 \end{cases} \quad (25)$$

$R_{f0}^S, R_{r0}^S, h_f^S, h_r^S, c_T^S, a_{f0}^S, a_{r0}^S, a_{f1}^S, a_{r1}^S$ , and  $n \in [0, 1]$  being positive material parameters, discussed in Section 4 (subscripts  $f$  and  $r$  stand for forward and reverse PT).

We remark that we derive such an expression by starting from some modeling contributions presented in the literature and cited in the above list. In particular, we distinguish between the positive and negative sign of  $B^S$  to model the asymmetric behavior between forward and reverse PTs. Then, we introduce the following terms: (i)  $h_f^S \chi^S$  and  $h_r^S \chi^S$  to classically describe hardening effects due to single-variant martensite; (ii)  $a_{f0}^S (\chi^S)^n$ ,  $a_{f1}^S (1 - \chi^S)^n$ ,  $a_{r0}^S (\chi^S)^n$ , and  $a_{r1}^S (1 - \chi^S)^n$  to describe hardening effects as well as smooth thermo-mechanical response always due to single-variant martensite; and (iii)  $c_T^S (T - T_0)$  to model increasing hysteresis width for low applied stresses in thermal-cycling tests at constant load as well as the width of the hysteresis loop in superelasticity decreasing with increasing temperature. This last choice manifests itself as two different slopes of the phase diagram boundaries for forward and reverse transformations, known as stress influence coefficients (Liang and Rogers, 1992) or stress rates (Duerig et al., 1990; Otsuka and Wayman, 1998), as presented in Section 4.

#### 2.1.4. Dissipation function

Although the proposed model relies on an yield surface-based formulation, we complete the description by recalling that the yield surface conditions can be equivalently converted in a pseudo-potential of dissipation,  $\phi = \phi(\dot{\chi}^M, \dot{\chi}^S, \dot{\mathbf{d}}^{tr})$ , which is a positive convex functional depending on dissipative variables, vanishing for vanishing dissipation, in particular in the form:

$$\phi = R^M |\dot{\chi}^M| + R^S |\dot{\chi}^S| + R^d \|\dot{\mathbf{d}}^{tr}\| \quad (26)$$

The introduced pseudo-potential of dissipation,  $\phi$ , captures forward and reverse austenite to multiple-variant martensite and austenite to single-variant martensite transformations as well as the reorientation process of single-variant martensite. The pseudo-potential of dissipation,  $\phi$ , may also depend on state and internal variables through the particular forms chosen for  $R^M$ ,  $R^S$ , and  $R^d$ . This choice assigns a significant flexibility to the model.

## 2.2. A SIMPLIFIED MODEL FORMULATION

Based on physically motivated considerations, the present Section introduces a simplified model formulation, based on a reduced set of material parameters but still able to capture fundamentals SMA feature effects.

### 2.2.1. Simplified Helmholtz free-energy function and time-continuous equations review

We start by making the following assumptions:

1. regarding single- and multiple-variant martensites, we reasonably assume:
  - equal internal energies and entropies between single- and multiple-variant martensites, implying  $\Delta u^{AMS} = \Delta u^{AM} = \Delta u^{AS}$  and  $\Delta s^{AMS} = \Delta s^{AM} = \Delta s^{AS}$ ;
  - equal interaction energies between single- and multiple-variant martensites with austenite, i.e.,  $\bar{\Psi}^{in} = \bar{\Psi}^{AM} = \bar{\Psi}^{AS}$  and  $\bar{\Psi}^{AMS} = \bar{\Psi}^{MS} = 0$ ;
  - equal shear moduli between single- and multiple-variant martensites, i.e.,  $G^{MS} = G^M = G^S$ ;
2. since many calorimetry experiments showed that the heat capacities of austenite and single-variant martensite are almost equal (Qidwai and Lagoudas, 2000), we assume  $\Delta c^{AS} = 0$ . We make the same reasonable assumption for multiple-variant martensite, i.e.,  $\Delta c^{AM} = 0$ ;
3. since  $T_0$  denotes the equilibrium temperature at which phases energy is equal, we choose  $T_0$  such that  $\Psi^{ch,A}(T_0) = \Psi^{ch,S}(T_0)$ , i.e.,  $T_0 = \Delta u^{AS} / \Delta s^{AS}$  (Sedláček et al., 2012). Since  $\Delta u^{AMS} = \Delta u^{AM} = \Delta u^{AS}$  and  $\Delta s^{AMS} = \Delta s^{AM} = \Delta s^{AS}$ , it follows  $\Delta u^{AMS} = \Delta s^{AMS} T_0$ .
4. since thermal expansion is a secondary effect compared to martensite production, we set the thermal expansion material coefficient,  $\alpha$ , equal to zero.

Then, by applying such assumptions to Eq. (14), we derive the free-energy function,  $\Psi^{simpl} = \Psi^{simpl}(\boldsymbol{\epsilon}, T, \chi^M, \chi^S, \mathbf{d}^{tr})$  (superscript *simpl* stands for simplified):

$$\begin{aligned}
\Psi^{simpl} = & \frac{1}{2} K \theta^2 + G \|\mathbf{e} - \varepsilon_L \chi^S \mathbf{d}^{tr}\|^2 \\
& + u_0^A - s_0^A T + c^A \left[ (T - T_0) - T \log \frac{T}{T_0} \right] \\
& + \Delta s^{AMS} (\chi^M + \chi^S) (T - T_0) + \bar{\Psi}^{in} (1 - \chi^M - \chi^S) (\chi^M + \chi^S) \\
& + I_{[0,1]}(\chi^M, \chi^S) + I_1(\|\mathbf{d}^{tr}\|)
\end{aligned} \tag{27}$$

We remark that the introduced free-energy function,  $\Psi^{simpl}$ , does not include full thermo-mechanical coupling since temperature is considered as a prescribed parameter.

A review of the model equations derived from the simplified free-energy (27) is reported in Table 1.

**TIME-CONTINUOUS SIMPLIFIED MODEL FRAME**

State variables:  $\boldsymbol{\epsilon}, T$

Internal variables:  $\chi^M, \chi^S, \mathbf{d}^{tr}$

Constraints on internal variables:

$$0 \leq \chi^M, \chi^S \leq 1, \quad \chi^M + \chi^S \leq 1, \quad \|\mathbf{d}^{tr}\| = 1$$

Constitutive equations:

$$\begin{cases} p = K\theta \\ \mathbf{s} = 2G(\mathbf{e} - \varepsilon_L \chi^S \mathbf{d}^{tr}) \\ \eta = s_0^A - \Delta s^{AMS}(\chi^M + \chi^S) + c^A \log \frac{T}{T_0} \end{cases}$$

$$\begin{cases} B^M = -\frac{\partial G}{\partial \chi^M} \|\mathbf{e} - \varepsilon_L \chi^S \mathbf{d}^{tr}\|^2 - \Delta s^{AMS}(T - T_0) \\ \quad - \bar{\Psi}^{in}(1 - 2\chi^M - 2\chi^S) - \gamma^M \\ B^S = 2G\varepsilon_L(\mathbf{e} - \varepsilon_L \chi^S \mathbf{d}^{tr}) : \mathbf{d}^{tr} - \frac{\partial G}{\partial \chi^S} \|\mathbf{e} - \varepsilon_L \chi^S \mathbf{d}^{tr}\|^2 \\ \quad - \Delta s^{AMS}(T - T_0) - \bar{\Psi}^{in}(1 - 2\chi^M - 2\chi^S) - \gamma^S \\ \mathbf{B}^d = 2G\varepsilon_L \chi^S (\mathbf{e} - \varepsilon_L \chi^S \mathbf{d}^{tr}) - \gamma^d \mathbf{d}^{tr} \end{cases}$$

Evolution equations:

$$\dot{\chi}^M = \dot{\zeta}^M \frac{B^M}{|B^M|}, \quad \dot{\chi}^S = \dot{\zeta}^S \frac{B^S}{|B^S|}, \quad \dot{\mathbf{d}}^{tr} = \dot{\zeta}^d \frac{\mathbf{B}^d}{\|\mathbf{B}^d\|}$$

Limit functions:

$$F^M = |B^M| - R^M, \quad F^S = |B^S| - R^S, \quad F^d = \|\mathbf{B}^d\| - R^d$$

Kuhn-Tucker conditions:

$$\begin{cases} \dot{\zeta}^M \geq 0, F^M \leq 0, \dot{\zeta}^M F^M = 0, \dot{\zeta}^M \dot{F}^M = 0 \\ \dot{\zeta}^S \geq 0, F^S \leq 0, \dot{\zeta}^S F^S = 0, \dot{\zeta}^S \dot{F}^S = 0 \\ \dot{\zeta}^d \geq 0, F^d \leq 0, \dot{\zeta}^d F^d = 0, \dot{\zeta}^d \dot{F}^d = 0 \end{cases}$$

Table 1: Time-continuous simplified model equations review

### 3. TIME-DISCRETE FRAME

We now elaborate on the algorithmic treatment of the model equations summarized in Table 1. For the sake of notation simplicity, the convention establishes superscript  $n$  for all the variables evaluated at time  $t_n$ , while drops superscript  $n + 1$  for all the variables computed at time  $t_{n+1}$ .

We start making use of a classical Backward-Euler integration algorithm for the evolution

equations (22). In this sense, time-discretized evolution equations are given by:

$$\begin{cases} \chi^M - \chi_n^M - \Delta\zeta^M \frac{B^M}{|B^M|} = 0 \\ \chi^S - \chi_n^S - \Delta\zeta^S \frac{B^S}{|B^S|} = 0 \\ \mathbf{d}^{tr} - \mathbf{d}_n^{tr} - \Delta\zeta^d \frac{\mathbf{B}^d}{\|\mathbf{B}^d\|} = 0 \end{cases} \quad (28)$$

where  $\Delta\zeta^M = \int_{t_n}^{t_{n+1}} \dot{\zeta}^M$ ,  $\Delta\zeta^S = \int_{t_n}^{t_{n+1}} \dot{\zeta}^S$  and  $\Delta\zeta^d = \int_{t_n}^{t_{n+1}} \dot{\zeta}^d$  are the time-integrated consistency parameters. Here Eq. (28)<sub>3</sub> guarantees constraint (4) through the indicator function presented in Eq. (13). All the remaining model equations are evaluated at time  $t_{n+1}$ .

In Section 1.2.3 we presented an overview of several numerical approaches available from the literature and suitable for both simple and more complex SMA phenomenological models. Since the purpose of the present paper to integrate the proposed constitutive equations is to reduce the complexity, and thus increase the efficiency, of the algorithmic treatment, this is achieved by eliminating the need for a predictor-corrector-type scheme and by automatically constraining the range of the variant volume fractions. In fact, in the resulting model, since we deal with several phase fractions, with strongly coupled evolutions and involving constraints, the application of standard predictor-corrector methods is not suitable, because an elaborate active set search has to be carried out. In particular, iterative solution procedures may suffer from instabilities caused by periodic oscillations of the active set.

An effective approach to the detection of an active set search has been introduced by Schmidt-Baldassari (2003) in the context of crystal plasticity, consisting in the replacement of the Kuhn-Tucker complementarity inequality conditions,  $a \leq 0$ ,  $b \geq 0$ ,  $ab = 0$ ,  $a, b \in \mathfrak{R}$ , by the equivalent Fischer-Burmeister complementarity function  $\Phi$  (Fischer, 1992), with  $\Phi : \mathfrak{R}^2 \rightarrow \mathfrak{R}$  and defined as follows:  $\Phi(a, b) = \sqrt{a^2 + b^2} + a - b$ , such that  $\Phi(a, b) = 0 \Leftrightarrow a \leq 0$ ,  $b \geq 0$ ,  $ab = 0$ . This general definition allows to rewrite the complementarity inequality constraints as a non-linear equality constraint by their replacement with a Fischer-Burmeister complementarity function. The application of Fischer-Burmeister functions makes possible to omit an active set search, a fundamental advantage when dealing with many coupled evolution equations.

The discrete Kuhn-Tucker conditions deriving from system (24) are so substituted by the following set of functions in the time-discrete frame:

$$\begin{cases} \sqrt{(F^M)^2 + (\Delta\zeta^M)^2} + F^M - \Delta\zeta^M = 0 \\ \sqrt{(F^S)^2 + (\Delta\zeta^S)^2} + F^S - \Delta\zeta^S = 0 \\ \sqrt{(F^d)^2 + (\Delta\zeta^d)^2} + F^d - \Delta\zeta^d = 0 \end{cases} \quad (29)$$

The same strategy can be employed to treat the set of inequalities given by constraint (2). In fact,

the additional Kuhn-Tucker conditions (21) can be substituted by the equivalent equalities:

$$\begin{cases} \sqrt{(\gamma^{M0})^2 + (\chi^M)^2} + \gamma^{M0} - \chi^M = 0 \\ \sqrt{(\gamma^{S0})^2 + (\chi^S)^2} + \gamma^{S0} - \chi^S = 0 \\ \sqrt{(\gamma^{MS})^2 + (\chi^M + \chi^S - 1)^2} - \gamma^{MS} + (\chi^M + \chi^S - 1) = 0 \end{cases} \quad (30)$$

The time-discrete problem, evaluated at time  $t_{n+1}$ , takes the specific form:

$$\mathbf{Q}(\boldsymbol{\epsilon}, \mathbf{h}) = \begin{bmatrix} \chi^M - \chi_n^M - \Delta\zeta^M \frac{B^M}{|B^M|} = 0 \\ \sqrt{(F^M)^2 + (\Delta\zeta^M)^2} + F^M - \Delta\zeta^M = 0 \\ \sqrt{(\gamma^{M0})^2 + (\chi^M)^2} + \gamma^{M0} - \chi^M = 0 \\ \chi^S - \chi_n^S - \Delta\zeta^S \frac{B^S}{|B^S|} = 0 \\ \sqrt{(F^S)^2 + (\Delta\zeta^S)^2} + F^S - \Delta\zeta^S = 0 \\ \sqrt{(\gamma^{S0})^2 + (\chi^M)^2} + \gamma^{S0} - \chi^S = 0 \\ \sqrt{(\gamma^{MS})^2 + (\chi^M + \chi^S - 1)^2} - \gamma^{MS} + (\chi^M + \chi^S - 1) = 0 \\ \mathbf{d}^{tr} - \mathbf{d}_n^{tr} - \Delta\zeta^d \frac{\mathbf{B}^d}{\|\mathbf{B}^d\|} = 0 \\ \sqrt{(F^d)^2 + (\Delta\zeta^d)^2} + F^d - \Delta\zeta^d = 0 \\ \|\mathbf{d}^{tr}\| - 1 = 0 \end{bmatrix} = \mathbf{0} \quad (31)$$

with  $\mathbf{h} = \{\chi^M, \Delta\zeta^M, \gamma^{M0}, \chi^S, \Delta\zeta^S, \gamma^{S0}, \gamma^{MS}, \mathbf{d}^{tr}, \Delta\zeta^d, \gamma^d\}$ . The active set can now be determined via the solution of the non-linear system of equations (31), using a classical Newton-Raphson method, which results in the standard update relation at iteration ( $k$ ), as follows:

$$\mathbf{h}^{(k+1)} = \mathbf{h}^{(k)} + \Delta\mathbf{h}^{(k)} \quad (32)$$

where:

$$\Delta\mathbf{h}^{(k)} = - \left( \frac{\partial \mathbf{Q}}{\partial \mathbf{h}} \right)^{-1} \mathbf{Q}(\boldsymbol{\epsilon}, \mathbf{h}^{(k)}) \quad (33)$$

The FE implementation of model equations and of all the numerical examples presented in Section 5 is carried out using the symbolic code generation system AceGen/AceFEM (Korelc, 2007). This system extends the symbolic capabilities of Mathematica (Wolfram, 2013) with the automatic differentiation technique, simultaneous optimization of expressions, and automatic generation of program code. Accordingly, we do not provide explicit expressions resulting from differentiation as these are obtained automatically using the automatic differentiation technique implemented in AceGen (Korelc, 2007). Application of these automation tools leads to exact linearization of the non-linear FE equations (consistent tangent matrix). This guarantees quadratic convergence rate

of the global Newton method and results in a robust and efficient FE implementation of the model, as illustrated by the numerical examples of Section 5.

We remark that, in cases where no analytical evaluation of the Jacobian matrix is possible, the most known approximation is through a finite difference scheme (Quarteroni et al., 2007). In such a case, to obtain good approximations of derivatives, the use of higher order divided difference is recommended, consequently leading to high computational costs in the evaluation of one or more residuals and to low efficiency.

Moreover, we observe that in the case of proportional loading, we may simplify model equations by setting  $\mathbf{d}^{tr} = \mathbf{s}/\|\mathbf{s}\|$ , as presented in Section 2.1.2. In such a case, system (31) is composed of only scalar-valued, rather than tensorial, equations by consequently increasing efficiency.

Since the Fischer-Burmeister complementary function,  $\Phi$ , is non-differentiable at  $(0, 0)$ , we introduce a regularized counterpart,  $\Phi_\delta$ , defined as  $\Phi_\delta(a, b, \delta) = \sqrt{a^2 + b^2 + 2\delta^2} + a - b$ , such that  $\Phi_\delta(a, b, \delta) = 0 \Leftrightarrow a \leq 0, b \geq 0, ab = -\delta^2$ , where  $\delta$  is a positive regularization parameter (Kanzow, 1996). This aspect characterizes especially the initiation of PTs, when both  $a$  and  $b$  are equal to zero.

Possible difficulties are linked to the numerical sensitiveness of these schemes (due to the presence of  $\delta$ ) and to the proper choice of the Newton-Raphson initial guess to guarantee a fast and correct convergence. In fact, a potential disadvantage of this method is that when the initial point is far from a solution, the method might not converge or may converge very slowly. To resolve these shortcomings, we apply a line-search strategy (Dennis and Schnabel, 1983; Nocedal and Wright, 1999). Such a choice is suggested by practical experience which reveals that it is not necessary to solve accurately for Eq. (33) to devise efficient methods (Quarteroni et al., 2007), rather, it is crucial to enforce some limitations on the step length such that:

$$\mathbf{h}^{(k+1)} = \mathbf{h}^{(k)} + \alpha^{(j)} \Delta \mathbf{h}^{(k)} \quad (34)$$

where  $\alpha^{(j)}$  represents the admissible coefficient at iteration  $(j)$  of the line-search procedure. Without introducing any limitation, a reasonable request on the choice of  $\alpha^{(j)}$  would seem to be that satisfying the following condition:

$$\|\mathbf{Q}(\boldsymbol{\epsilon}, \mathbf{h}^{(k+1)})\| < \|\mathbf{Q}(\boldsymbol{\epsilon}, \mathbf{h}^{(k)})\| \quad (35)$$

for which the new iterate,  $\mathbf{h}^{(k+1)}$ , satisfies the inequality when  $\mathbf{h}^{(k)}$  and  $\Delta \mathbf{h}^{(k)}$  have been fixed. To this purpose, a simple procedure, that starts from a sufficiently large value of the step length,  $\alpha^{(j)}$ , and halves this value until condition (35) is fulfilled, can be used even if not always satisfactory (Dennis and Schnabel, 1983). In fact, more stringent criteria than condition (35) have to be adopted in the choice of possible values for  $\alpha^{(j)}$  to avoid a slow descent rate of the sequence and the use of small step sizes. Among the most up-to-date strategies, we adopt here the back-tracking line-search technique for which the following condition needs to be satisfied (Quarteroni et al., 2007):

$$\|\mathbf{Q}(\boldsymbol{\epsilon}, \mathbf{h}^{(k+1)})\| < \|\mathbf{Q}(\boldsymbol{\epsilon}, \mathbf{h}^{(k)})\| + \lambda \alpha^{(j)} \frac{\partial \mathbf{Q}}{\partial \mathbf{h}} \Delta \mathbf{h}^{(k)} \quad (36)$$

with  $\lambda \in (0, 0.5)$ . In our case, the procedure, that starts from a sufficiently large value of the step length,  $\alpha^{(j)}$ , and halves this value until condition (36) is fulfilled, has been demonstrated effective

and efficacy. Clearly, other strategies can be used for the choice of  $\alpha^{(j)}$  and theoretical results can be found in the well-known book by Dennis and Schnabel (1983).

The application of the Fischer-Burmeister algorithm to the proposed problem leads to a well-behaved and robust algorithmic scheme as demonstrated by examples described in Section 5. Table 2 provides a summary of the full algorithm needed to integrate the constitutive relations in a FE framework, while Table 3 presents the numerical scheme for the adopted line-search strategy, where we assume  $\lambda = 10^{-4}$  and  $\rho = 0.5$ .

Moreover, in Eq. (25) we choose  $R^S$  such that its derivatives become infinite as  $\chi^S$  approaches 0 or 1 to ensure a smooth transition in stress-strain or strain-temperature response predicted at initiation and completion of transformation. While this condition is essentially an analytical one, the numerical evaluation of these derivatives at  $\chi^S = 0$  and  $\chi^S = 1$  may cause computational difficulties. To avoid this problem, we introduce a modification of  $R^S$  as follows:

$$R^S = \begin{cases} R_{f0}^S + h_f^S \chi^S + a_{f0}^S (\chi^S + \epsilon)^n + a_{f1}^S (1 - \chi^S + \epsilon)^n & \text{if } B^S \geq 0 \\ R_{r0}^S - h_r^S \chi^S - c_T^S (T - T_0) + a_{r0}^S (\chi^S + \epsilon)^n + a_{r1}^S (1 - \chi^S + \epsilon)^n & \text{if } B^S < 0 \end{cases} \quad (37)$$

$\epsilon$  being a positive regularization parameter. For small values of  $\epsilon$  (e.g.,  $\epsilon = 10^{-8}$ ), Eq. (37) produces results similar to those provided by Eq. (25).

---

1. Initialize

**i.** Set  $k = 0$ ,  $\mathbf{h}^{(0)} = (\chi_n^M; \Delta\zeta_n^M; \gamma_n^{M0}; \chi_n^S; \Delta\zeta_n^S; \gamma_n^{S0}; \gamma_n^{MS}; \mathbf{d}_n^{tr}; \Delta\zeta_n^d; \gamma_n^d)$  at time  $t_{n+1}$

2. Determination of the solution

Repeat

**i.** Compute  $B^{S(k)} = B^S(\boldsymbol{\epsilon}, T, \mathbf{h}^{(k)})$  at time  $t_{n+1}$

**ii.** Compute  $R^{S(k)} = R^S(B^{S(k)}, \mathbf{h}^{(k)}, T)$  at time  $t_{n+1}$

**iii.** Find  $\Delta\mathbf{h}^{(k)}$  solving system (31) via Newton-Raphson scheme through Eq. (33)

**iv.** Evaluate  $\mathbf{h}^{(k+1)}$  by applying a line-search strategy (see Table 3)

**v.** Set  $k = k + 1$

until  $\|\mathbf{Q}(\boldsymbol{\epsilon}, \mathbf{h}^{(k)})\| < tol$

---

Table 2: Full algorithm to integrate the constitutive relations of the proposed model.

- 
1. Choose  $\lambda \in (0, 0.5)$  and  $\rho \in (0, 1)$
  2. Set  $j = 0, \alpha^{(0)} = 1$
  3. Compute  $\mathbf{h}^{(k+1)} = \mathbf{h}^{(k)} + \alpha^{(0)} \Delta \mathbf{h}^{(k)}$
  4. While  $\|\mathbf{Q}(\boldsymbol{\epsilon}, \mathbf{h}^{(k+1)})\| > \|\mathbf{Q}(\boldsymbol{\epsilon}, \mathbf{h}^{(k)})\| + \lambda \alpha^{(j)} \frac{\partial \mathbf{Q}}{\partial \mathbf{h}} \Delta \mathbf{h}^{(k)}$  do
    - i.  $\alpha^{(j+1)} = \rho \alpha^{(j)}$
    - ii.  $\mathbf{h}^{(k+1)} = \mathbf{h}^{(k)} + \alpha^{(j+1)} \Delta \mathbf{h}^{(k)}$
    - iii.  $j = j + 1$
  5. End
- 

Table 3: Back-tracking line-search algorithm.

#### 4. MODEL CALIBRATION

This Section is dedicated to the calibration of the proposed model. To properly calibrate most of the model parameters it is sufficient to focus on one-dimensional stress states, condition which reduces the model to the following simplified form:

$$\Psi^{1D} = \frac{1}{2} \frac{\sigma^2}{E} + u_0^A - s_0^A T + c^A \left[ (T - T_0) - T \log \frac{T}{T_0} \right] + \Delta s^{AMS} (\chi^M + \chi^S) (T - T_0) \quad (38)$$

$$+ \bar{\Psi}^{in} (1 - \chi^M - \chi^S) (\chi^M + \chi^S) + I_{[0,1]} (\chi^M, \chi^S)$$

where  $\sigma$  is the uniaxial state of stress and  $E$  is the Young's modulus defined in terms of the elastic modulus of austenite,  $E^A$ , and of the elastic modulus of martensite,  $E^{MS}$ , as follows:

$$\frac{1}{E} = (1 - \chi^M - \chi^S) \frac{1}{E^A} + (\chi^M + \chi^S) \frac{1}{E^{MS}} \quad (39)$$

In the following, for the sake of calculus simplicity, we assume  $E = E^A = E^{MS}$ .

Then, we can derive the thermodynamic forces,  $B^M$  and  $B^S$ , as follows:

$$\begin{cases} B^M = -\Delta s^{AMS} (T - T_0) - \bar{\Psi}^{in} (1 - 2\chi^M - 2\chi^S) - \gamma^M \\ B^S = \varepsilon_L \sigma - \Delta s^{AMS} (T - T_0) - \bar{\Psi}^{in} (1 - 2\chi^M - 2\chi^S) - \gamma^S \end{cases} \quad (40)$$

Moreover, we recall the adopted expression for  $R^S$ :

$$R^S = \begin{cases} R_{f0}^S + h_f^S \chi^S + a_{f0}^S (\chi^S)^n + a_{f1}^S (1 - \chi^S)^n & \text{if } B^S \geq 0 \\ R_{r0}^S - h_r^S \chi^S - c_T^S (T - T_0) + a_{r0}^S (\chi^S)^n + a_{r1}^S (1 - \chi^S)^n & \text{if } B^S < 0 \end{cases} \quad (41)$$

In the following, we firstly present the one-dimensional stress-temperature phase diagram related to the proposed model. Then, we list the model parameters to be calibrated, we indicate possible calibration techniques and we also comment, whenever possible, on their physical interpretation. Moreover, for a complete overview, we cite some other works from the literature, which adopt the same physical interpretation for some parameters of the proposed model. In particular, we observe that:

- the elastic moduli ( $E^A$  and  $E^{MS}$ , with the corresponding three-dimensional quantities,  $G^A$ ,  $G^{MS}$ , and  $K$ ) and the maximum amount of single-variant martensite,  $\varepsilon_L$ , can be determined directly from experimental uniaxial stress-strain curves at constant temperature;
- the difference of entropy between the austenitic and single-variant martensitic phases,  $\Delta s^{AMS}$ , can be determined from the slope of the forward phase transformation curve in a stress-temperature space, usually obtained from experimental tensile tests (Qidwai and Lagoudas, 2000; Sedláč et al., 2012). Its determination is deepened in Section 4.3;
- the material parameter,  $c_T^S$ , describes the change of the hysteresis loop width in superelasticity (i.e., the difference between upper and lower plateau stress), which decreases with

increasing temperature, as experimentally demonstrated by Sittner et al. (2009) and also modeled, for instance, in the work by Sedláč et al. (2012). Its determination from the slope of the reverse phase transformation curve in a stress-temperature space, usually obtained from experimental tensile tests, is reported in Section 4.3;

- the material constant indicating interaction energies between phases,  $\overline{\Psi}^{in}$ , the equilibrium temperature,  $T_0$ , and the parameters related to the transformation radii, i.e.,  $R^M$ ,  $R_{f*}^S$ ,  $R_{r*}^S$ ,  $h_f^S$ ,  $h_r^S$ , can be easily calibrated by considering a temperature-induced transformation under zero stress and a stress-induced transformation at high temperature;
- the parameters  $a_{f0}^S$ ,  $a_{r0}^S$ ,  $a_{f1}^S$ ,  $a_{r1}^S$ , and exponent,  $n$ , of Eq. (25) or (41), do not have an associated material property and are directly chosen to best fit the four corners of the transformation hysteresis plots.

In the following, we consider only the governing equations of the two transformations necessary to model calibration, i.e., a temperature-induced transformation under zero stress and a stress-induced transformation at high temperature. Moreover, for the sake of calculus simplicity, we assume  $R^S$  as follows:

$$R^S = \begin{cases} R_{f0}^S + h_f^S \chi^S & \text{if } B^S \geq 0 \\ R_{r0}^S - h_r^S \chi^S - c_T^S (T - T_0) & \text{if } B^S < 0 \end{cases} \quad (42)$$

#### 4.1. PHASE DIAGRAM OF THE PROPOSED MODEL

This Section presents the one-dimensional stress-temperature phase diagram related to the proposed model and shown in Figure 1(a).

To simplify the presentation, the three phases are denoted by  $A$ ,  $M$  and  $S$ , standing for austenite, multi- and single-variant martensites, respectively. The five possible PTs, indicated in Figure 1(a), are denoted by  $A \rightarrow M$ ,  $A \rightarrow S$ ,  $M \rightarrow A$ ,  $S \rightarrow A$ , and  $M \rightarrow S$  for austenite to multi-variant martensite, austenite to single-variant martensite, multi-variant martensite to austenite, single-variant martensite to austenite and multi- to single-variant martensite, respectively.

The critical start and finish transformation temperatures at zero stress level are denoted as follows:  $M_s$  and  $M_f$  for the  $A \rightarrow M$  transformation,  $A_s^M$  and  $A_f^M$  for the  $M \rightarrow A$  transformation,  $S_s$  and  $S_f$  for the  $A \rightarrow S$  transformation, and  $A_s^S$  and  $A_f^S$  for the  $S \rightarrow A$  transformation.  $A_s^S$  and  $A_f^S$  are assumed as different from  $A_s^M$  and  $A_f^M$  in agreement with experiments provided by Popov and Lagoudas (2007). All the temperatures are indicated in Figure 1(a), except for  $S_s$  and  $S_f$ .

The critical uniaxial start and finish stresses required for detwinning of twinned martensite, i.e., transformation  $M \rightarrow S$ , are denoted by  $\sigma_s$  and  $\sigma_f$ , respectively.

The phase diagram of Figure 1(a) follows the established literature in assuming three regions where only the pure phases  $A$ ,  $M$  and  $S$  can exist (light-blue shaded regions of Figure 1(a)). The three regions are separated by transformation strips which are labeled according to the transformations which take place. Note that some of these strips overlap and in an overlap region multiple transformations are possible. In the non-shaded region of the phase diagram various mixtures can exist (white regions of Figure 1(a)).

Due to the lack of inelastic strain associated with the  $A \leftrightarrow M$  transformation, we assume the start and finish lines for the forward and reverse transformations  $A \leftrightarrow M$  vertical and passing through the critical temperatures  $M_s$ ,  $M_f$ ,  $A_s^M$  and  $A_f^M$ , respectively (Leclercq and LExcellent, 1996; Popov and Lagoudas, 2007). This assumption has been adopted in several models taking into account the separate development of single- and multiple-variant martensites, e.g., for instance, (Leclercq and LExcellent, 1996; Popov and Lagoudas, 2007). Clearly, the two strips are bounded by the critical stress,  $\sigma_f$ .

The start and finish lines for the forward strip  $A \rightarrow S$  pass through the critical temperatures  $S_s$  and  $S_f$  and exhibits a temperature dependence, defined by the positive slope,  $k_f$ , in Figure 1(a). Equivalently, the start and finish lines for the reverse strip  $S \rightarrow A$  pass through the critical temperatures  $A_s^S$  and  $A_f^S$  and exhibits a temperature dependence, defined by the positive slope,  $k_r$ . Moreover, the two strips present different widths. These features are due to the fact that the present flexible model takes into account for: (i) different kinetics between forward and reverse PTs; (ii) the increasing hysteresis width for low applied stresses in thermal-cycling tests at constant load; and (iii) the width of the hysteresis loop in superelasticity decreasing with increasing temperature.

Since Popov and Lagoudas (2007) demonstrated that if the finish line for the  $A \rightarrow S$  strip passes above the intersection point  $(M_s, \sigma_f)$  then one can find a particular isobaric cooling path which leads to jump discontinuities in the strain as the temperature is lowered, we assume the finish line for the  $A \rightarrow S$  strip passing through or below the point  $(M_s, \sigma_f)$  (in Figure 1(a) the extreme case is represented by an orange dot). Furthermore, two approaches are available from the literature for the definition of the  $A \rightarrow S$  strip at low stresses ( $\sigma < \sigma_s$ ) and temperatures ( $T < M_s$ ): some authors have extended it to zero-stress level (Bekker and Brinson, 1997); others (Lagoudas and Shu, 1999) suggest that in the region  $T < M_s$  the dependence on temperature disappears and there is a critical stress below which  $A \rightarrow S$  does not occur. In our case, we assume the first choice reasonable.

Now, we consider the simple phase diagram related to the model by Souza et al. (1998) and shown in Figure 1(b), which classically describes the behavior of SMAs material in a one-dimensional setting. The model considers the presence of only two possible phase fractions, i.e., austenite and single-variant martensite, as shown in Figure 1(b). As clearly explained in Section 1, the model is unable to catch SMA behavior for work conditions where the material is considered as linear elastic and where the model is particularly sensitive to its numerical implementation. Such a work condition includes stress values lower than  $\sigma_f$  at  $T < T_0$ , as it can be observed in Figure 1(b). Contrarily, the proposed model allows for a more flexible approach taking into account the presence of multiple PTs and PTs at low levels of stress.

#### 4.2. TEMPERATURE-INDUCED TRANSFORMATION

We start considering a temperature-induced transformation under zero stress. To this purpose, Figure 2 focuses only on the  $A \leftrightarrow M$  transformation, by highlighting the two related vertical strips (orange regions). Accordingly, exploiting the definition (40)<sub>1</sub> for the driving force  $B^M$ , we can detect start and finish of forward and reverse PT through the following conditions:

- Start forward PT:  $F^M|_{T=M_s} = -\Delta s^{AMS}(M_s - T_0) - \bar{\Psi}^{in} - R^M = 0$
- Finish forward PT:  $F^M|_{T=M_f} = -\Delta s^{AMS}(M_f - T_0) + \bar{\Psi}^{in} - R^M = 0$

- Start reverse PT:  $F^M|_{T=A_s^M} = -\Delta s^{AMS}(A_s^M - T_0) + \bar{\Psi}^{in} + R^M = 0$
- Finish reverse PT:  $F^M|_{T=A_f^M} = -\Delta s^{AMS}(A_f^M - T_0) - \bar{\Psi}^{in} + R^M = 0$

where  $M_s, M_f, A_s^M$  and  $A_f^M$  can be easily determined by differential scanning calorimetry (DSC) tests (Popov and Lagoudas, 2007; Qidwai and Lagoudas, 2000). We assume  $T_0 = (M_f + A_f^M)/2$ , i.e., we treat  $T_0$  as equilibrium temperature. Accordingly, since forward and reverse PTs are perfectly symmetric, we derive  $R^M$  and  $\bar{\Psi}^{in}$  by considering only the two equations related to forward PT:

$$\begin{cases} \bar{\Psi}^{in} = -\frac{\Delta T^{AM} \Delta s^{AMS}}{2} \\ R^M = \Delta s^{AMS} \left( \Delta T_0 + \frac{\Delta T^{AM}}{2} \right) \end{cases} \quad (43)$$

where  $\Delta T^{AM} = M_s - M_f = A_f^M - A_s^M$  and  $\Delta T_0 = T_0 - M_s = A_s^M - T_0$  (see Figure 2).

#### 4.3. STRESS-INDUCED TRANSFORMATION

We now consider a stress-induced transformation at constant high temperature,  $T^*$ . To this purpose, Figure 3 focuses only on  $A \leftrightarrow S$  transformation, by highlighting the related strips (orange regions). The loading path is represented in Figure 3 by a vertical violet line passing through  $T^*$ .

Accordingly, exploiting the definition (40)<sub>2</sub> for the driving force  $B^S$ , we can detect start and finish of forward and reverse PT through the following conditions:

- Start forward PT:  $F^S|_{\sigma=\sigma_s^S} = \varepsilon_L \sigma_s^S - \Delta s^{AMS}(T^* - T_0) - \bar{\Psi}^{in} - R_{f0}^S = 0$
- Finish forward PT:  $F^S|_{\sigma=\sigma_f^S} = \varepsilon_L \sigma_f^S - \Delta s^{AMS}(T^* - T_0) + \bar{\Psi}^{in} - R_{f0}^S - h_f^S = 0$
- Start reverse PT:  $F^S|_{\sigma=\sigma_s^A} = \varepsilon_L \sigma_s^A - \Delta s^{AMS}(T^* - T_0) + \bar{\Psi}^{in} + R_{r0}^S - h_r^S - c_T^S(T^* - T_0) = 0$
- Finish reverse PT:  $F^S|_{\sigma=\sigma_f^A} = \varepsilon_L \sigma_f^A - \Delta s^{AMS}(T^* - T_0) - \bar{\Psi}^{in} + R_{r0}^S - c_T^S(T^* - T_0) = 0$

where  $\sigma_s^S, \sigma_f^S, \sigma_s^A$  and  $\sigma_f^A$  are the martensitic and austenitic start and finish stresses, respectively. The transformation lines for forward and reverse transformations are linear with slopes  $k_f = \Delta s^{AMS}/\varepsilon_L$  and  $k_r = (\Delta s^{AMS} + c_T^S)/\varepsilon_L$ , respectively (see Figure 3). Once  $k_f$  and  $k_r$  are experimentally determined, we can calibrate both  $\Delta s^{AMS}$  and  $c_T^S$ .

Finally, we deduce the remaining model parameters by considering the four equations, as follows:

$$\begin{cases} h_f^S = \varepsilon_L \Delta \sigma^S + 2\bar{\Psi}^{in} \\ h_r^S = \varepsilon_L \Delta \sigma^A + 2\bar{\Psi}^{in} \\ R_{f0}^S = \varepsilon_L \sigma_s^S - \bar{\Psi}^{in} - \Delta s^{AMS}(T^* - T_0) \\ R_{r0}^S = (\Delta s^{AMS} + c_T^S)(T^* - T_0) + \bar{\Psi}^{in} - \varepsilon_L \sigma_f^A \end{cases} \quad (44)$$

where  $\Delta \sigma^S = \sigma_f^S - \sigma_s^S$  and  $\Delta \sigma^A = \sigma_s^A - \sigma_f^A$  (see Figure 3).

## 5. NUMERICAL SIMULATIONS AND EXPERIMENTAL VALIDATIONS

In this Section we test the validity of the model as well as algorithm efficiency through several numerical simulations and comparisons with experimental results on thin superelastic NiTi wires reported by Sittner et al. (2009). Then, we approach a complex three-dimensional finite element analysis of a real SMA-based device, i.e., an helical spring actuator.

In all the numerical tests we adopt the material parameters reported in Table 4 and calibrated as described in Section 4, by referring to the material properties characterizing NiTi wires and provided by Pilch et al. (2009); Sittner et al. (2009); in particular, the material parameters are extracted from an experimental curve, i.e., a tensile test at a constant temperature of 10 °C (Figure 4).

It is important to notice that all the parameters are calibrated using only uniaxial data. The reduced number of experimental data for the calibration certainly reduces the model accuracy, but the purpose is to emphasize: (i) model prediction capabilities, based on a simple calibration method, through a quantitative validation with experimental data; and, above all, (ii) the robustness and efficiency of the adopted numerical procedure, through a more complex three-dimensional analysis of a real SMA-based device.

In all the simulations, to emphasize the improvements of the new modeling framework, we compare the proposed model with the model by Souza et al. (1998) (Auricchio et al., 2009b).

### 5.1. ISO-THERMAL TENSILE TESTS

We start considering uniaxial tensile tests at constant temperature, simulated as simple uniaxial tension tests, with displacement control and prescribed homogeneous constant temperature field. We consider four constant temperatures of 40, 20, -10 and -20 °C for the tensile tests and four constant temperatures of 40, 20, 10 and -20 °C for the tensile tests with internal subloops. Accordingly, Figures 5 and 6 report stress-strain diagrams. Compared to the model by Souza et al. (1998), the proposed model allows for an accurate description of material behavior by reproducing experimental hysteresis loops decreasing with increasing temperature, transformation-dependent elastic properties as well as PTs smoothness.

### 5.2. THERMAL-CYCLING TESTS AT CONSTANT APPLIED STRESSES

We now present thermal-cycling tests at constant stress, simulated as uniaxial tension tests with load control and prescribed homogeneous varying temperature field. We consider two constant stresses of 300 and 400 MPa. Accordingly, Figure 7 reports strain-temperature diagrams. The experimental curves are successfully predicted by both models for  $\sigma = 400$  MPa, while both models fail for  $\sigma = 300$  MPa since an experimental weak inelastic strain is obtained for low stress levels. Although there is no clear experimental evidence, these small actuation strains can be attributed to a R-phase transformation (Sittner et al., 2009), not taken into account by both models. Another clear feature of the proposed model is the decrease of temperature hysteresis width with increasing stress.

Parameter	Value	Unit	Parameter	Value	Unit
$G^A$	21890	MPa	$R^M$	1	MPa
$G^{MS}$	9016	MPa	$R_{f0}^S$	1	MPa
$K$	31125	MPa	$R_{r0}^S$	17	MPa
$\varepsilon_L$	6.15	%	$h_f^S$	1	MPa
$T_0$	-48.15	°C	$h_r^S$	1	MPa
$\Delta_s^{AMS}$	0.31	MPa/°C	$a_{f0}^S$	2	MPa
$\overline{\Psi}^{in}$	-0.1	MPa	$a_{f1}^S$	0.5	MPa
$c_T^S$	0.2	MPa/°C	$a_{r0}^S$	0.01	MPa
$n$	0.1	/	$a_{r1}^S$	9	MPa

Table 4: Model parameters used in all the numerical simulations.

### 5.3. THERMO-MECHANICAL RECOVERING STRESS TESTS

We now present thermo-mechanical recovering stress tests carried out on a wire strained in tension at room temperature, up to a certain level of prestrain, at upper and lower plateau, respectively, followed by thermal-cycling at constant prestrain and final unloading at room temperature. Again, the present tests are simulated as uniaxial tension tests. We consider a room temperature of 24 °C and three levels of prestrain of 2%, 3.5% and 5%. Accordingly, Figures 8-9 represent stress-strain (left) and stress-temperature (right) diagrams at both upper and lower plateau. The transformation slopes as well as the achieved magnitude of the recovery stress at maximum temperature predicted by the proposed model are in good agreement with experiments also if both models do not capture the absence of hysteresis in the stress-temperature plot.

### 5.4. COMBINED TENSION-TORSION TESTS

We present results of combined tension-torsion tests consisting of iso-thermal loading paths with applied angular displacement at constant axial stress. The numerical prediction are obtained considering a 1 mm wire segment, modeled using 8-node brick FE discretization consisting in one element through the wire thickness and 320 elements in the cross-section.

Accordingly, Figure 10 represents torque-angular displacement (left) and axial strain-angular displacement (right) diagrams. Tests in the first row of Figure 10 are performed at a constant tensile stress of 70 MPa and at a constant temperature of 30 °C; curves in the second row are plotted for a constant tensile stress of 194 MPa and at a constant temperature of 40 °C; curves in the third row are plotted for a constant tensile stress of 379 MPa and at a constant temperature of 40 °C.

Both models underpredict the resulting torque moment and overestimate the maximum amount of transformation strain reached at the end of the transformation. However, discrepancies are not surprising since all the material parameters are calibrated using uniaxial tests. In fact, thin wires loaded in tension often exhibit a localization of transformation, which produces more well stress-oriented variants, resulting in an important transformation strain in tension. In torsion test, due to the stress gradient through the radius, no localization is expected and, consequently, a reduced transformation strain is expected. As the models consider the transformation in an average way, this kind of effects is not captured. Moreover, there are discrepancies in terms of axial strains, due to the effect of strong material texture and anisotropy, not accounted by isotropic models, which influences yield transformation surfaces and transformation strains (Sittner et al., 2009). In fact, tension/compression asymmetry, which is accounted for in the model by Souza et al. (1998), originates from the transformation anisotropy associated with NiTi cubic to monoclinic martensitic transformation (Sittner et al., 2009). The model by Souza et al. (1998) nevertheless remains isotropic and hence the tension/compression asymmetry does not solve the problem of the length of the plateau in angular displacements in torsion. Beside these discrepancies, the global behavior of the proposed model is generally in good agreement with experiments.

### 5.5. SIMULATION OF SMA DEVICE

We conclude this Section by considering a real SMA-based device, i.e., an SMA helical spring actuator. Such device constitutes an important example of actuator and, despite the apparent simplicity, its behavior is rather complex. Consequently, its design may possibly take advantage of

numerical simulations. The literature presents numerous efforts for the modeling, design, simulation and control of SMA actuator systems related to innovative devices employed for different purposes. Among them, there have been several efforts to model SMA helicoidal springs thermo-mechanical behavior (Attanasi et al., 2011; de Aguiar et al., 2013, 2010; Dumont and Kuhl, 2005; Saleeb et al., 2013a; Savi and Braga, 1993; Toi et al., 2004).

The SMA helical spring actuator considered in the present work consists of 3.5 free coils of initial length of 24.59 mm, a wire diameter of 1.5 mm, a spring external diameter of 13.3 mm, a spring internal diameter of 10.3 mm and a pitch size of 6.4 mm. Figure (11) reports the adopted mesh, consisting of 6912 8-node brick elements and 7497 nodes, and the initial geometry.

First, we simulate a helical spring at a constant temperature of 40 °C. We apply an axial force at the bottom end of the helical spring while the top end is completely fixed. We increase the force from zero to its maximum value and then, we unload the force back to zero. We remark that all the nodes on the bottom section are constrained against the two translations in the directions orthogonal to the axial one (thus ensuring that the bottom section is restrained against twist rotation). Figure 12(a) shows the deformed shape under the maximum force, compared to the initial geometry of the spring. After unloading, the spring recovers its original shape as expected in the PE regime. Figure 12(b) shows the force-vertical displacement (of the loaded end) diagram. The results presented in Figure 12(b) illustrate also the robustness of the present formulation and implementation. The markers indicate the solution obtained using large load increments (automatic step size control <sup>1</sup>), whereas the solid line corresponds to fixed small load increments. As it can be seen, the former solution follows exactly the latter. To assess computational efficiency of the present model and its FE implementation, Table 5 provides the total number of steps, the total number of global Newton iterations and the total computation time for both the small and large load increments.

Then, to qualitatively compare the behavior of the proposed model to that by Souza et al. (1998) for low-stress PTs, we consider the spring fixed at the top end, initially loaded by a vertical force at the bottom end and subjected to temperature cycle while keeping constant the load. We consider two constant loads of 5 and 15 N. Figures 13(a) and 13(c) show the two loading histories during the simulations, while Figures 13(b) and 13(d) show the vertical displacement-temperature diagrams. As it can be observed, compared to the model by Souza et al. (1998), the proposed model is able to capture low-stress PTs and to predict the decrease of temperature hysteresis width with increasing stress (see Figures 13(b)-(d)).

## 6. CONCLUSIONS

The present paper has developed a refined and general three-dimensional phenomenological constitutive model for SMAs, taking into account several physical phenomena. Moreover, the present paper has proposed the numerical implementation of the new model, through an effective and efficient procedure, consisting in the replacement of the classical set of Kuhn-Tucker conditions by the Fischer-Burmeister complementarity function. The great advantage of the numerical

---

<sup>1</sup>All computations are performed using an automatic step size control procedure in which the desired number of Newton iterations is prescribed (here, equal to 8), and the current load increment is increased (decreased) when the number of iterations at the previous increment is smaller (larger) than the desired number.

algorithms based on the Fischer-Burmeister complementary functions is that no active set search is required, allowing an efficient procedure for complex constitutive models. Numerical robustness and efficiency have been carefully investigated. Possible difficulties and the adopted solutions have been described. Extensive numerical tests have been performed to show robustness as well as efficiency of the proposed integration algorithm and the quantitative validation of the proposed model with experimental data has been addressed to confirm model reliability.

Type of load increments	Number of steps	Number of iterations	Total time [s]
Large	52	401	909.046
Fine	204	1023	2134.75

Table 5: Pseudoelastic test of a SMA helical spring actuator: comparison of computational efficiency.

## Acknowledgement

This work is partially funded by the Ministero dell'Istruzione, dell'Università e della Ricerca through the Project no. 2010BFXRHS.

## References

- Arghavani, J., Auricchio, F., Naghdabadi, R., Reali, A., 2011. On the robustness and efficiency of integration algorithms for a 3D finite strain phenomenological SMA constitutive model. *Int. J. Numer. Methods Eng.* 85, 107–134.
- Arghavani, J., Auricchio, F., Naghdabadi, R., Reali, A., Sohrabpour, S., 2010. A 3D phenomenological constitutive model for shape memory alloys under multiaxial loadings. *Int. J. Plasticity* 26, 976–991.
- Attanasi, G., Auricchio, F., Urbano, M., 2011. Theoretical and Experimental Investigation on SMA Superelastic Springs. *J. Mater. Eng. Perform.* 20 (4-5), 706–711.
- Auricchio, F., Bonetti, E., 2013. A new flexible 3D macroscopic model for shape memory alloys. *Discrete Contin. Dyn. Syst. Ser. S* 6 (2), 277–291.
- Auricchio, F., Coda, A., Reali, A., Urbano, M., 2009a. SMA numerical modeling versus experimental results: parameter identification and model prediction capabilities. *J. Mater. Eng. Perform.* 18, 649–654.
- Auricchio, F., Conti, M., Morganti, S., Reali, A., 2010a. Shape Memory Alloy: from Constitutive Modeling to Finite Element Analysis of Stent Deployment. *CMES* 57 (3), 225–243.
- Auricchio, F., Morganti, S., Reali, A., 2009b. SMA numerical modeling versus experimental results. In: *Proceedings of European Symposium on Martensitic Transformations (ESOMAT 2009)*. pp. 1–6.
- Auricchio, F., Petrini, L., 2004a. A three-dimensional model describing stress-temperature induced solid phase transformations: solution algorithm and boundary value problems. *Int. J. Numer. Methods Eng.* 6, 807–836.
- Auricchio, F., Petrini, L., 2004b. A three-dimensional model describing stress-temperature induced solid phase transformations: thermomechanical coupling and hybrid composite applications. *Int. J. Numer. Methods Eng.* 61, 716–737.
- Auricchio, F., Reali, A., Stefanelli, U., 2007. A three-dimensional model describing stress-induced solid phase transformation with permanent inelasticity. *Int. J. Plasticity* 23, 207–226.
- Auricchio, F., Reali, A., Tardugno, A., 2010b. Shape-memory alloys: effective 3D modelling, computational aspects and design of devices. *Int. J. Comp. Mat. Sc. Surf. Eng.* 3, 199–223.
- Auricchio, F., Stefanelli, U., 2004. Numerical Analysis of a three-dimensional super-elastic constitutive model. *Int. J. Numer. Methods Eng.* 61, 142–155.
- Azaouzi, M., Lebaal, N., Makradi, A., Belouettar, S., 2013. Optimization based simulation of self-expanding Nitinol stent. *Materials and Design* 50, 917–928.
- Bartel, T., Hackl, K., 2009. A micromechanical model for martensitic transformations in shape-memory alloys based on energy relaxation. *ZAMM* 89, 792–809.
- Bartel, T., Hackl, K., 2010. Multiscale modeling of martensitic phase transformations: on the numerical determination of heterogeneous mesostructures within shape-memory alloys induced by precipitates. *Techn. Mech.* 30, 324–342.

- Bartel, T., Menzel, A., Svendsen, B., 2011. Thermodynamic and relaxation-based modeling of the interaction between martensitic phase transformations and plasticity. *J. Mech. Phys. Solids* 59, 1004–1019.
- Bekker, A., Brinson, L., 1997. Temperature-induced phase transformation in a shape memory alloy: phase diagram based kinetics approach. *J. Mech. Phys. Solids* 45 (6), 949–988.
- Bouvet, C., Calloch, S., LExcellent, C., 2002. Mechanical behavior of a Cu-Al-Be shape memory alloy under multi-axial proportional and nonproportional loadings. *J. Eng. Mater-T. ASME* 124, 112–124.
- Bouvet, C., Calloch, S., LExcellent, C., 2004. A phenomenological model for pseudoelasticity of shape memory alloys under multiaxial proportional and nonproportional loadings. *Eur. J. Mech. A-Solid* 23, 37–61.
- Brinson, L., 1993. One-dimensional constitutive behavior of shape memory alloys: thermomechanical derivation with non-constant material functions and redefined martensite internal variables. *J. Intel. Mat. Syst. Str.* 4, 229–242.
- Chemisky, Y., Chatzigeorgiou, G., Kumar, P., Lagoudas, D., 2014. A constitutive model for cyclic actuation of high-temperature shape memory alloys. *Mech. Mater.* 68, 120–136.
- Chemisky, Y., Duval, A., Patoor, E., Ben Zineb, T., 2011. Constitutive model for shape memory alloys including phase transformation, martensitic reorientation and twins accommodation. *Mech. Mater.* 43, 361–376.
- de Aguiar, R., de Castro Leo Neto, W., Savi, M., Calas Lopes Pacheco, P., 2013. Shape memory alloy helical springs performance: Modeling and experimental analysis. *Materials Science Forum* 758, 147–156.
- de Aguiar, R., Savi, M., Pacheco, P., 2010. Experimental and numerical investigations of shape memory alloy helical springs. *Smart Mater. Struct.* 19, 1–9.
- Dennis, J., Schnabel, R., 1983. *Numerical Methods for Unconstrained Optimization and Nonlinear Equations*. Prentice-Hall, Englewood Cliffs, New York.
- Duerig, T., Melton, K., Stoekel, D., Wayman, C., 1990. *Engineering Aspects of Shape Memory Alloys*. Butterworth-Heinemann, London.
- Dumont, G., Kuhl, C., 2005. Finite element simulation for design optimization of shape memory alloy spring actuators. *Eng. Computation* 22, 835–848.
- Fischer, A., 1992. A special Newton-type optimization method. *Optim.* 24, 269–284.
- Frémond, M., 2002. *Non-smooth Thermomechanics*. Springer-Verlag, Berlin.
- Gao, X., Qiao, R., Brinson, L., 2007. Phase diagram kinetics for shape memory alloys: a robust finite element implementation. *Smart Mater. Struct.* 16, 2102–2115.
- Grabe, C., Bruhns, O., 2009. Path dependence and multiaxial behavior of a polycrystalline NiTi alloy within the pseudoelastic and pseudoplastic temperature regimes. *Int. J. Plasticity* 25, 513–545.
- Gurtin, M., Fried, E., Anand, L., 2010. *The Mechanics and Thermodynamics of Continua*. Vol. 158. Cambridge University Press.
- Hartl, D., , Lagoudas, D., 2009. Constitutive modeling and structural analysis considering simultaneous phase transformation and plastic yield in shape memory alloys. *Smart Mater. Struct.* 18, 1–17.
- Hartl, D., Chatzigeorgiou, G., Lagoudas, D., 2010. Three-dimensional modeling and numerical analysis of rate-dependent irrecoverable deformation in shape memory alloys. *Int. J. Plasticity* 26, 1485–1507.

- Helm, D., 2007. Numerical simulation of martensitic phase transitions in shape memory alloys using an improved integration algorithm. *Int. J. Numer. Methods Eng.* 69, 1997–2035.
- Helm, D., Haupt, P., 2003. Shape memory behaviour: modelling within continuum thermomechanics. *Int. J. Solids Struct.* 40 (4), 827–849.
- Huang, W., 1998. Shape Memory Alloys and their Application to Actuators for Deployable Structures. Ph.D. thesis, University of Cambridge.
- Kanzow, C., 1996. Some noninterior continuation methods for linear complementarity problems. *SIAM J. Matrix Anal. Appl.* 17, 851–868.
- Khandelwal, A., Buravalla, V., 2009. Models for shape memory alloy behavior: An overview of modeling approaches. *Int. J. Struct. Changes Sol.* 1, 111–148.
- Kiefer, B., Bartel, T., , Menzel, A., 2012. Implementation of numerical integration schemes for the simulation of magnetic SMA constitutive response. *Smart Mater. Struct.* 21, 1–8.
- Korelc, J., 2007. AceFEM/AceGen Manual 2007. <http://www.fgg.uni-lj.si/Symech/>.
- Lagoudas, D., Bo, Z., Qidwai, M., 1996. A unified thermodynamic constitutive model for SMA and finite element analysis of active metal matrix composites. *Mech. Compos. Mater. St.* 3 (2), 153–179.
- Lagoudas, D., Entchev, P., Popov, P., Patoor, E., Brinson, L., Gao, X., 2006. Shape memory alloys, Part II: Modeling of polycrystals. *Mech. Mater.* 38, 430–462.
- Lagoudas, D., Shu, S., 1999. Residual deformations of active structures with SMA actuators. *Int. J. Mech. Sci.* 41, 595–619.
- Lagoudas, D. C., Hartl, D., Chemisky, Y., Machado, L., Popov, P., 2012. Constitutive model for the numerical analysis of phase transformation in polycrystalline shape memory alloys. *Int. J. Plasticity* 32-33, 155–183.
- Leclercq, S., LExcellent, C., 1996. A general macroscopic description of the thermomechanical behavior of shape memory alloys. *Journal of the Mechanics and Physics of Solids* 44, 953–980.
- LExcellent, C., Boubakar, M., Bouvet, C., Calloch, S., 2006. About modelling the shape memory alloy behaviour based on the phase transformation surface identification under proportional loading and anisothermal conditions. *Int. J. Solids Struct.* 48, 613–626.
- LExcellent, C., Leclercq, S., Gabry, B., Bourbon, G., 2000. The two way shape memory effect of shape memory alloys: an experimental study and a phenomenological model. *Int. J. Plasticity* 16, 1155–1168.
- Liang, C., Rogers, C., 1992. Design of shape memory alloy actuators. *J. Mech. Design* 114, 223.
- Lim, T., McDowell, D., 1999. Mechanical behavior of an Ni-Ti shape memory alloy under axial-torsional proportional and nonproportional loading. *J. Eng. Mater.-T. ASME* 121, 9–18.
- Lubliner, J., 1990. *Plasticity theory*. MacMillan, New York.
- Luig, P., Bruhns, O., 2008. On the modeling of shape memory alloys using tensorial internal variables. *Mat. Sci. Eng. A-Struct.* 481-482, 379–383.
- Morin, C., Moumni, Z., Zaki, W., 2011a. A constitutive model for shape memory alloys accounting for thermomechanical coupling. *Int. J. Plasticity* 27, 748–767.

- Morin, C., Moumni, Z., Zaki, W., 2011b. Thermomechanical coupling in shape memory alloys under cyclic loadings: Experimental analysis and constitutive modeling. *Int. J. Plasticity* 27 (12), 1959–1980.
- Moumni, Z., Zaki, W., Nguyen, Q., 2008. Theoretical and numerical modeling of solid-solid phase change: Application to the description of the thermomechanical behavior of shape memory alloys. *Int. J. Plasticity* 24, 614–645.
- Nocedal, J., Wright, S., 1999. *Numerical Optimization*. Springer.
- Otsuka, K., Ren, X., 2005. Physical metallurgy of Ti-Ni-based shape memory alloys. *Prog. Mater. Sci.* 50, 511–678.
- Otsuka, K., Wayman, C., 1998. *Shape Memory Materials*. Cambridge University Press, Cambridge.
- Panico, M., Brinson, L., 2007. A three-dimensional phenomenological model for martensite reorientation in shape memory alloys. *J. Mech. Phys. Solids* 55 (11), 2491–2511.
- Panoskaltsis, V., Bahuguna, S., Soldatos, D., 2004. On the thermomechanical modeling of shape memory alloys. *Int. J. NonLinear Mech.* 39 (5), 709–722.
- Panoskaltsis, V., Soldatos, D., Triantafyllou, S., 2011a. A new model for shape memory alloy materials under general states of deformation and temperature conditions. In: Boudouvis, A., Stavroulakis, G. (Eds.), *Proceedings of the 7th GRACM International Congress on Computational Mechanics*.
- Panoskaltsis, V., Soldatos, D., Triantafyllou, S., 2011b. Generalized Plasticity Theory for Phase Transformations. *Procedia Eng.* 10, 3104–3108, [;ce:title;11th International Conference on the Mechanical Behavior of Materials \(ICM11\);/ce:title;](#)
- Patoor, E., Lagoudas, D., Entchev, P., Brinson, L., Gao, X., 2006. Shape memory alloys, Part I: General properties and modeling of single crystals. *Mech. Mater.* 38, 391–429.
- Peigney, M., Seguin, J., 2013. An incremental variational approach to coupled thermo-mechanical problems in anelastic solids. Application to shape-memory alloys. *Int. J. Solids Struct.* xx (-), xx–xx.
- Peigney, M., Seguin, J., Herve-Luanco, E., 2011. Numerical simulation of shape memory alloys structures using interior-point methods. *Int. J. Solids Struct.* 48, 2791–2799.
- Peng, X., Chen, B., Chen, X., Wang, J., Wang, H., 2012. A constitutive model for transformation, reorientation and plastic deformation of shape memory alloys. *Acta Mech. Solida Sin.* 25 (3), 285–298.
- Peultier, B., Ben Zineb, T., Patoor, E., 2006. Macroscopic constitutive law for SMA: Application to structure analysis by FEM. *Mech. Mater.* 38, 510–524.
- Peultier, B., Ben Zineb, T., Patoor, E., 2008. A simplified micromechanical constitutive law adapted to the design of shape memory applications by finite element methods. *Mat. Sci. Eng. A-Struct.* 481-482, 384–388.
- Pilch, J., Heller, L., Sittner, P., 2009. <http://department.fzu.cz/ofm/roundrobin>.
- Popov, P., Lagoudas, D., 2007. A 3D constitutive model for shape memory alloys incorporating pseudoelasticity and detwinning of self-accommodated martensite. *Int. J. Plasticity* 23, 1679–1720.
- Qidwai, M., Lagoudas, D., 2000. On thermomechanics and transformation surfaces of polycrystalline NiTi shape memory alloy material. *Int. J. Plasticity* 16, 1309–1343.
- Quarteroni, A., Sacco, R., Saleri, F., 2007. *Numerical Mathematics*. Springer.
- Raniecki, B., Lexcelent, C., Tanaka, K., 1992. Thermodynamic models of pseudoelastic behaviour of shape memory

- alloys. *Arch. Mech.* 44, 261–284.
- Rockafellar, R., 1970. *Convex Analysis*. Princeton University Press, Princeton.
- Saint-Sulpice, L., Arbab Chirani, S., Calloch, S., 2009. A 3D super-elastic model for shape memory alloys taking into account progressive strain under cyclic loadings. *Mech. Mater.* 41, 12–26.
- Saleeb, A., Dhakal, B., Hosseini, M., Padula II, S., 2013a. Large scale simulation of NiTi helical spring actuators under repeated thermomechanical cycles. *Smart Mater. Struct.* 22, 1–20.
- Saleeb, A., Dhakal, B., Padula II, S., Gaydosch, D., 2013b. Calibration of a three-dimensional multimechanism shape memory alloy material model for the prediction of the cyclic attraction character in binary NiTi alloys. *J. Intel. Mat. Syst. Str.* 4, 70–88.
- Saleeb, A., Padula, S., Kumar, A., 2011. A multi-axial, multimechanism based constitutive model for the comprehensive representation of the evolutionary response of SMAs under general thermomechanical loading conditions. *Int. J. Plasticity* 5, 655–687.
- Savi, M., Braga, A., 1993. Chaotic vibrations of an oscillator with shape memory. *J. Braz. Soc. Mech. Sci. & Eng.* 15, 1–20.
- Schmidt-Baldassari, M., 2003. Numerical concepts for rate-independent single crystal plasticity. *Comput. Methods in Appl. Mech. Eng.* 192, 1261–1280.
- Sedláč, P., Frost, M., Benešová, B., Ben Zineb, T., Šittner, P., 2012. Thermomechanical model for NiTi-based shape memory alloys including R-phase and material anisotropy under multi-axial loadings. *Int. J. Plasticity* 39, 132–151.
- Shaw, J., Kyriakides, S., 1995. Thermomechanical aspects of NiTi. *J. Mech. Phys. Solids* 43 (8), 1243–1281.
- Sittner, P., Hara, Y., Tokuda, M., 1995. Experimental study on the thermoelastic martensitic transformation in shape memory alloy polycrystal induced by combined external forces. *Metall. Mater. Trans. A* 26, 2923–2935.
- Sittner, P., Heller, L., Pilch, J., Sedlak, P., Frost, M., Chemisky, Y., Duval, A., Piotrowski, B., Ben Zineb, T., Patoor, E., Auricchio, F., Morganti, S., Reali, A., Rio, G., Favier, D., Liu, Y., Gibeau, E., LExcellent, C., Boubakar, L., Hartl, D., Oehler, S., Lagoudas, D., Van Humbeeck, J., 2009. Round robin SMA modeling. In: Sittner, P., Heller, L., Paidar, V. (Eds.), *The 8th European Symposium on Martensitic Transformations (ESOMAT 2009)*. EDP Sciences, p. 08001.
- Souza, A., Mamiya, E., Zouain, N., 1998. Three-dimensional model for solids undergoing stress-induced phase transformations. *Eur. J. Mech. A-Solid* 17, 789–806.
- Stachowiak, G., McCormick, P., 1987. Two stage yielding in a NiTi alloy. *Scripta Metall. Mater.* 21, 403–406.
- Stachowiak, G., McCormick, P., 1988. Shape memory behaviour associated with the R and martensitic transformations in a NiTi alloy. *Mater. T. JIM* 36 (2), 291–297.
- Stupkiewicz, S., Petryk, H., 2012. A robust model of pseudoelasticity in shape memory alloys. *Int. J. Numer. Methods Eng.* 93 (7), 747–769.
- Sun, Q., Li, Z., 2002. Phase transformation in superelastic NiTi polycrystalline micro-tubes under tension and torsion - from localization to homogeneous deformation. *Int. J. Solids Struct.* 39, 3797–3809.
- Thamburaja, P., Anand, L., 2001. Polycrystalline shape-memory materials: effect of crystallographic texture. *J. Mech. Phys. Solids* 49, 709–737.

- Toi, Y., Lee, J., Taya, M., 2004. Finite element analysis of superelastic, large deformation behavior of shape memory alloy helical springs. *Comput. Struct.* 82, 1685–93.
- Wagner, M., Windl, W., 2008. Lattice stability, elastic constants and macroscopic moduli of NiTi martensites from first principles. *Acta Mater.* 56, 6232–6245.
- Williams, E., Elahina, M., 2008. An Automotive SMA Mirror Actuator: Modeling, Design, and Experimental Evaluation. *Journal of Intelligent Material Systems and Structures* 19, 1425–1434.
- Wolfram, 2013. *Mathematica Documentation*, [www.wolfram.com](http://www.wolfram.com).
- Wu, W., Qi, M., Liu, X., Yang, D., Wang, W., 2007. Delivery and Release of Nitinol Stent in Carotid Artery and their Interactions: a Finite Element Analysis. *J. Biomech.* 40, 3034–3040.
- Zaki, W., 2012a. An efficient implementation for a model of martensite reorientation in martensitic shape memory alloys under multiaxial nonproportional loading. *Int. J. Plasticity* 37, 72–94.
- Zaki, W., 2012b. Time integration of a model for martensite detwinning and reorientation under nonproportional loading using Lagrange multipliers. *Int. J. Solids Struct.* 49 (21), 2951–2961.
- Zaki, W., Moumni, Z., 2007a. A 3D model of the cyclic thermomechanical behavior of shape memory alloys. *J. Mech. Phys. Solids* 55 (11), 2427–2454.
- Zaki, W., Moumni, Z., 2007b. A three-dimensional model of the thermomechanical behavior of shape memory alloys. *J. Mech. Phys. Solids* 55 (11), 2455–2490.
- Zaki, W., Zamfir, S., Moumni, Z., 2010. An extension of the ZM model for shape memory alloys accounting for plastic deformation. *Mech. Mater.* 42, 266–274.

## LIST OF FIGURES.

- Figure 1: 1D phase diagrams generated by (a) the proposed model and (b) the Souza model, in terms of stress,  $\sigma$ , and temperature,  $T$ .
- Figure 2: Identification of model parameters from a temperature-induced transformation.
- Figure 3: Identification of model parameters from a stress-induced transformation.
- Figure 4: Model calibration on a tensile test at a constant temperature of 10 °C.
- Figure 5: Model response for iso-thermal tensile tests.
- Figure 6: Model response for iso-thermal tensile tests with internal subloops.
- Figure 7: Model response for thermal-cycling tests at constant tensile stresses.
- Figure 8: Model response for thermo-mechanical recovering stress tests at upper plateau.
- Figure 9: Model response for thermo-mechanical recovering stress tests at lower plateau.
- Figure 10: Model response for combined tension-torsion tests.
- Figure 11: SMA helical spring actuator: adopted mesh.
- Figure 12: Pseudoelastic test of a SMA helical spring actuator: (a) spring initial geometry and scaled deformed shape under the maximum force (color map indicates distribution of the single-variant martensite volume fraction,  $\chi^S$ ); (b) force vs. vertical displacement of the loaded end of the spring diagram (markers, large load increments; solid line, small increments).
- Figure 13: Thermal-cycling test at constant load of a SMA helical spring actuator: (a)-(c) temperature and force loading histories during simulation; (b)-(d) vertical displacement of the loaded end of the spring vs. temperature diagrams.

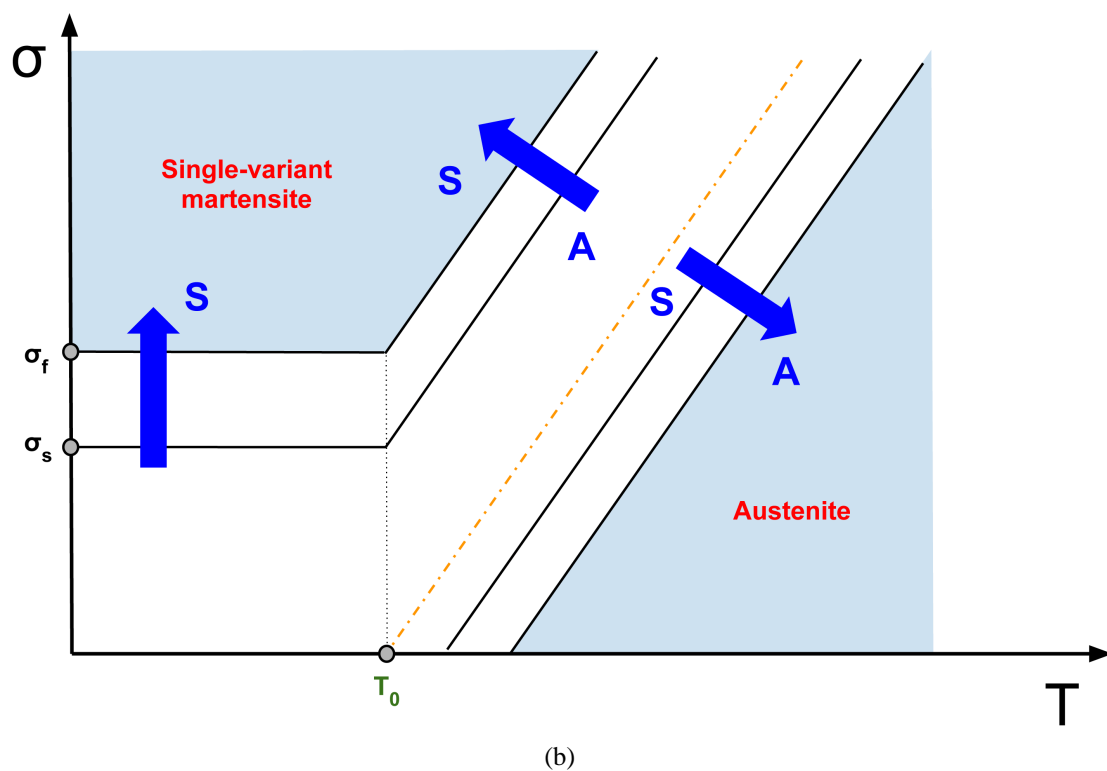
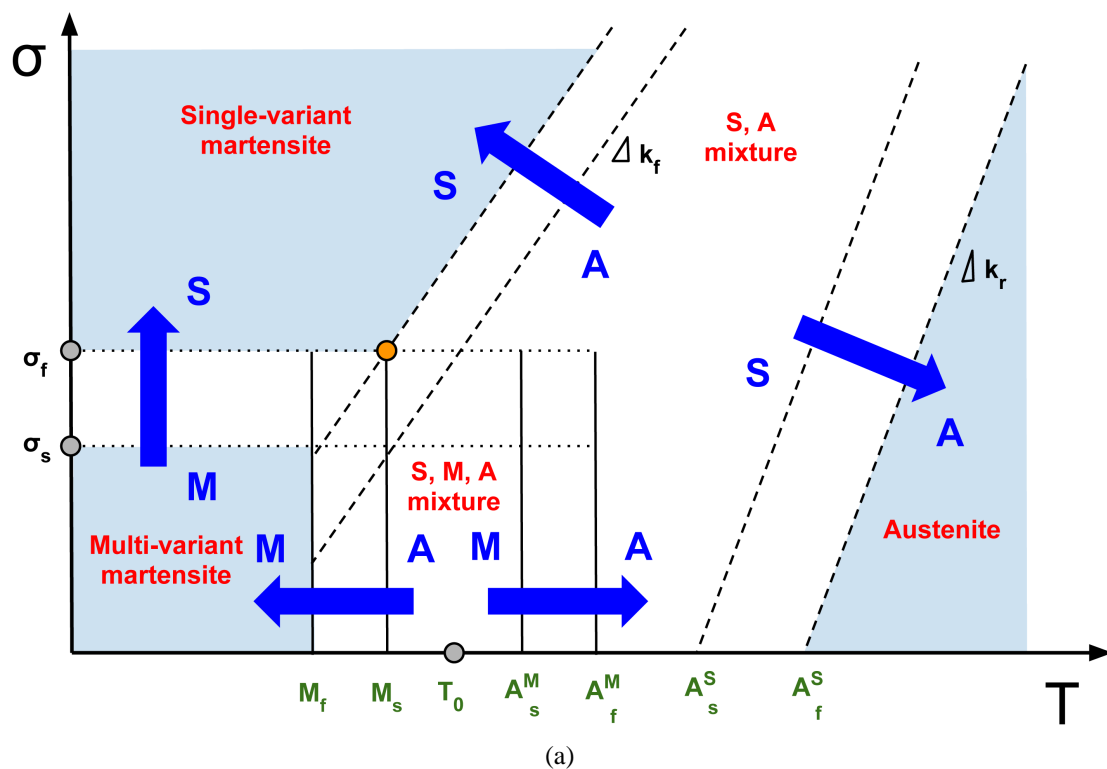


Figure 1: 1D phase diagrams generated by (a) the proposed model and by (b) Souza model, in terms of stress,  $\sigma$ , and temperature,  $T$ .

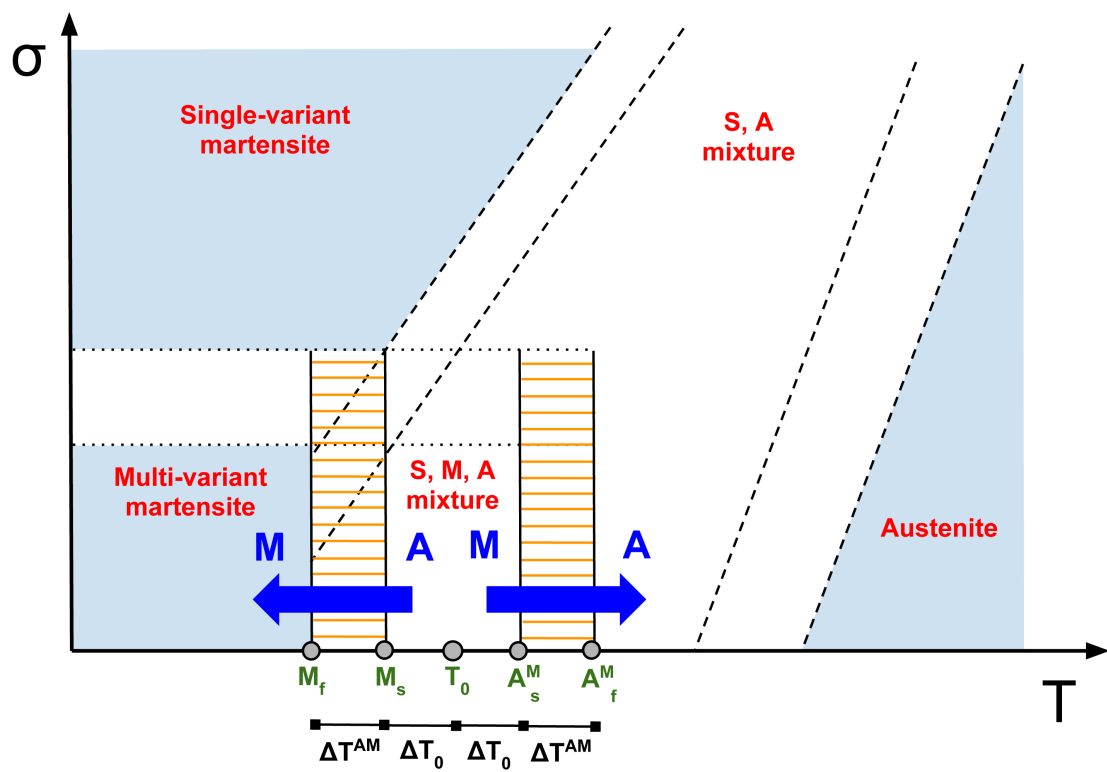


Figure 2: Identification of model parameters from a temperature-induced transformation.

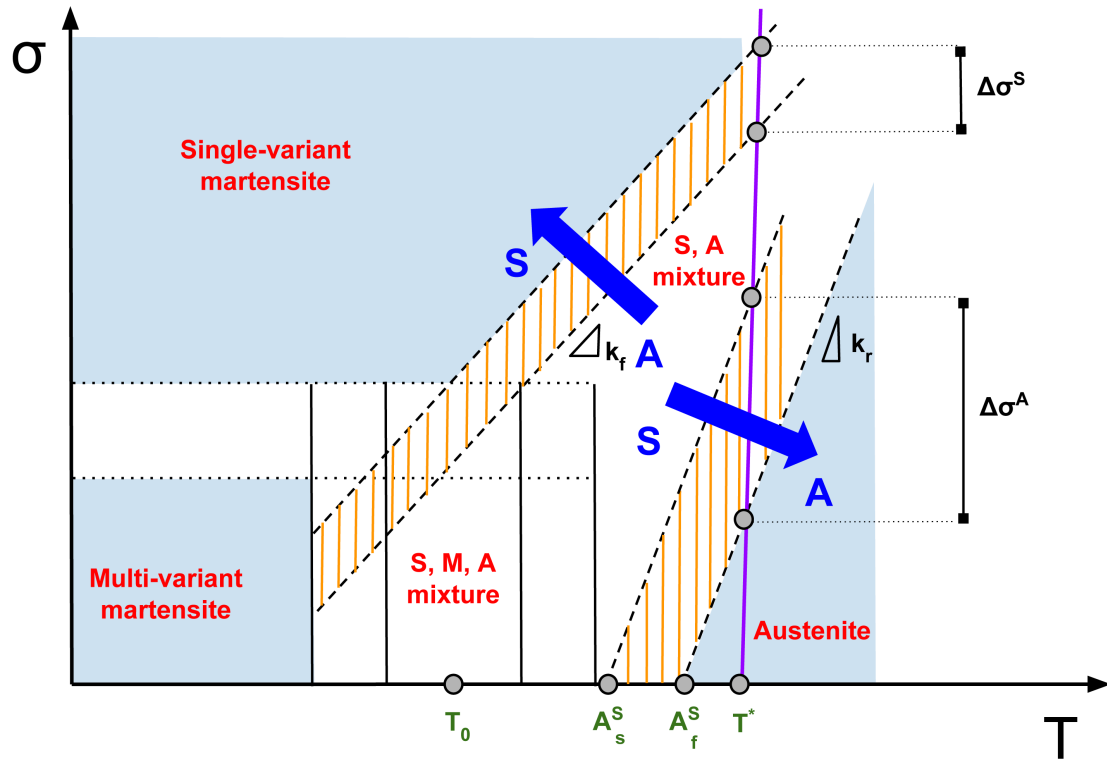


Figure 3: Identification of model parameters from a stress-induced transformation.

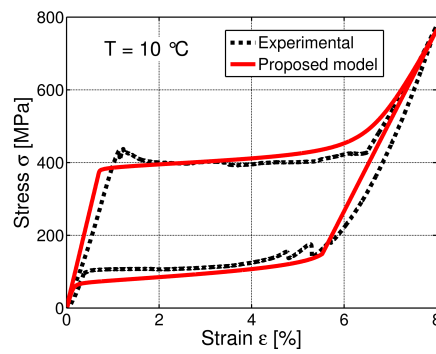


Figure 4: Model calibration on a tensile test at a constant temperature of  $10^\circ\text{C}$ .

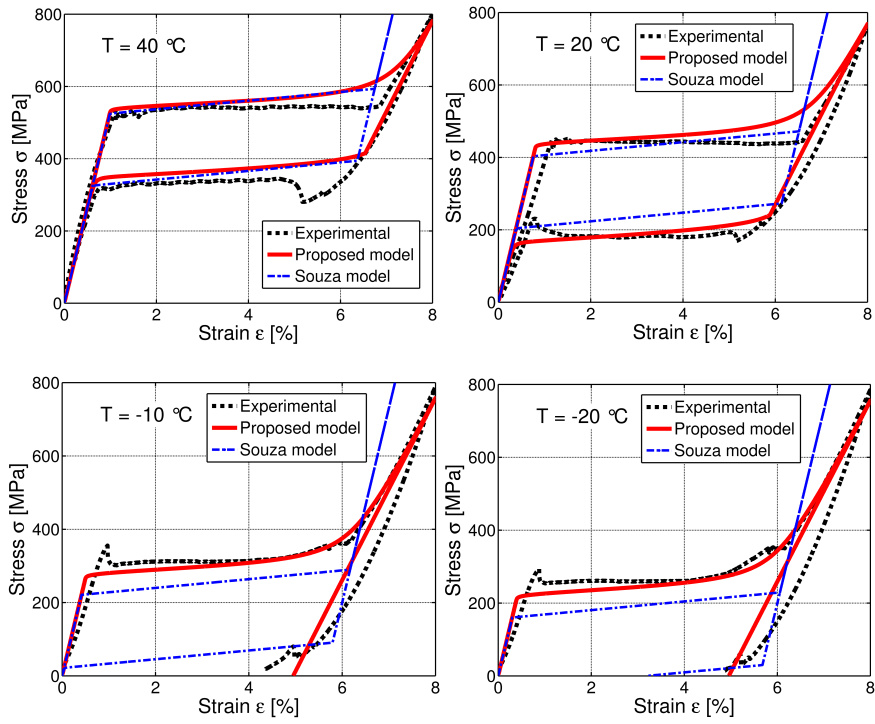


Figure 5: Model response for iso-thermal tensile tests.

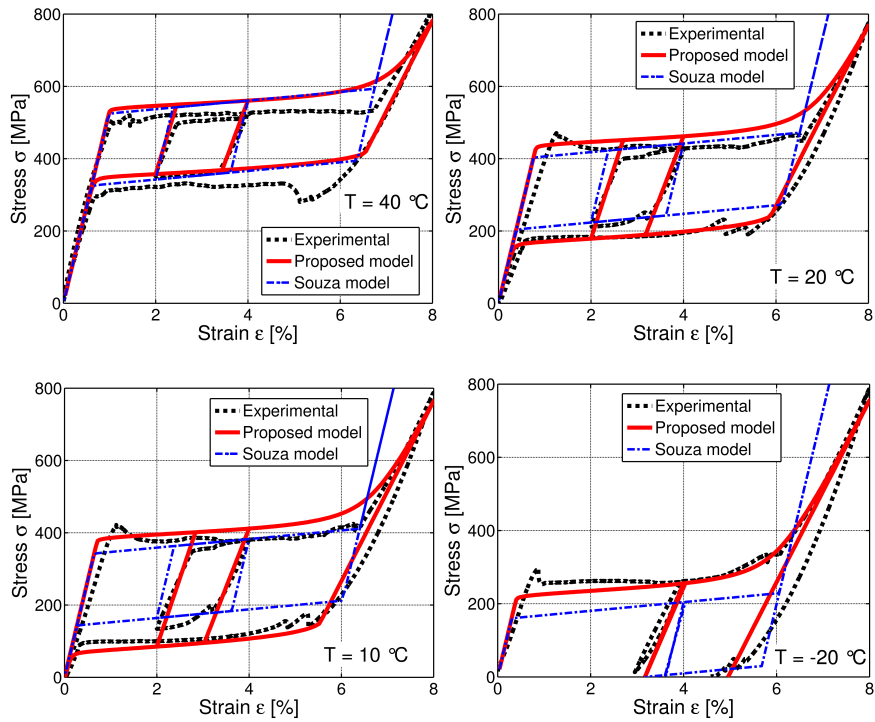


Figure 6: Model response for iso-thermal tensile tests with internal subloops.

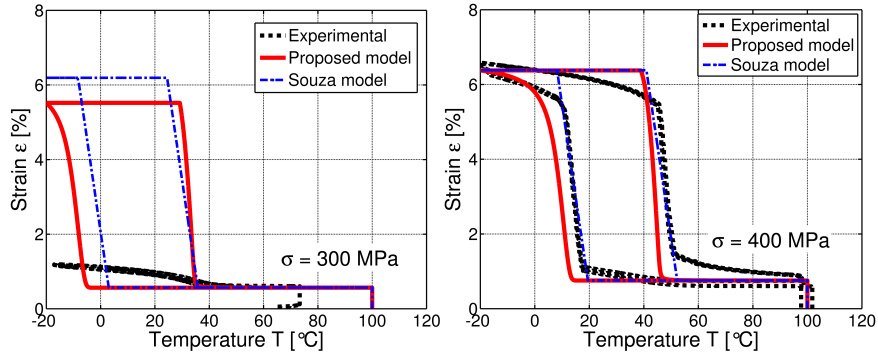


Figure 7: Model response for thermal-cycling tests at constant tensile stresses.

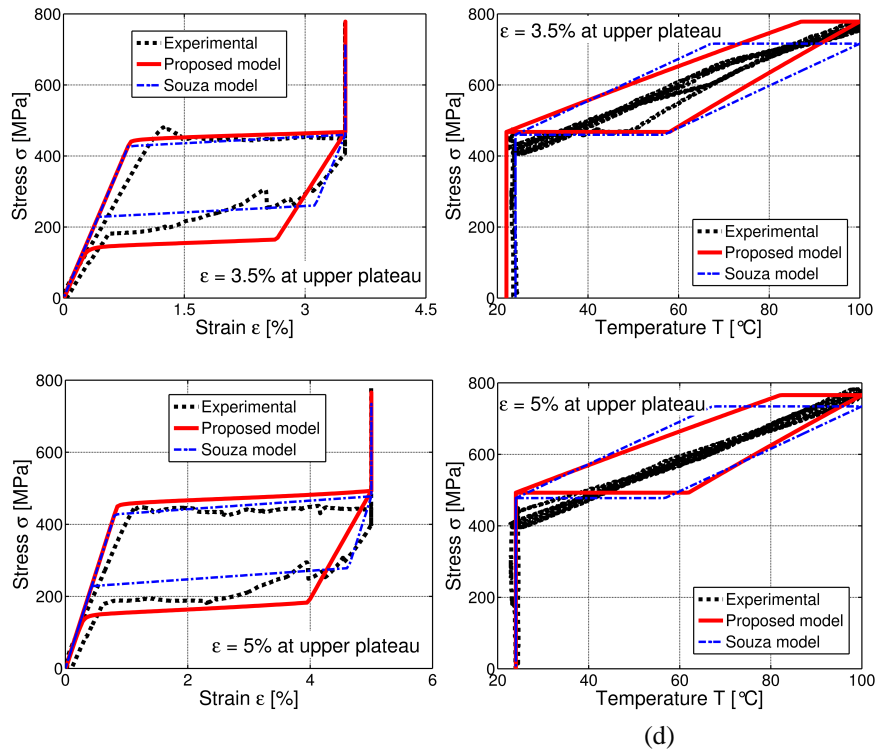


Figure 8: Model response for thermo-mechanical recovering stress tests at upper plateau.

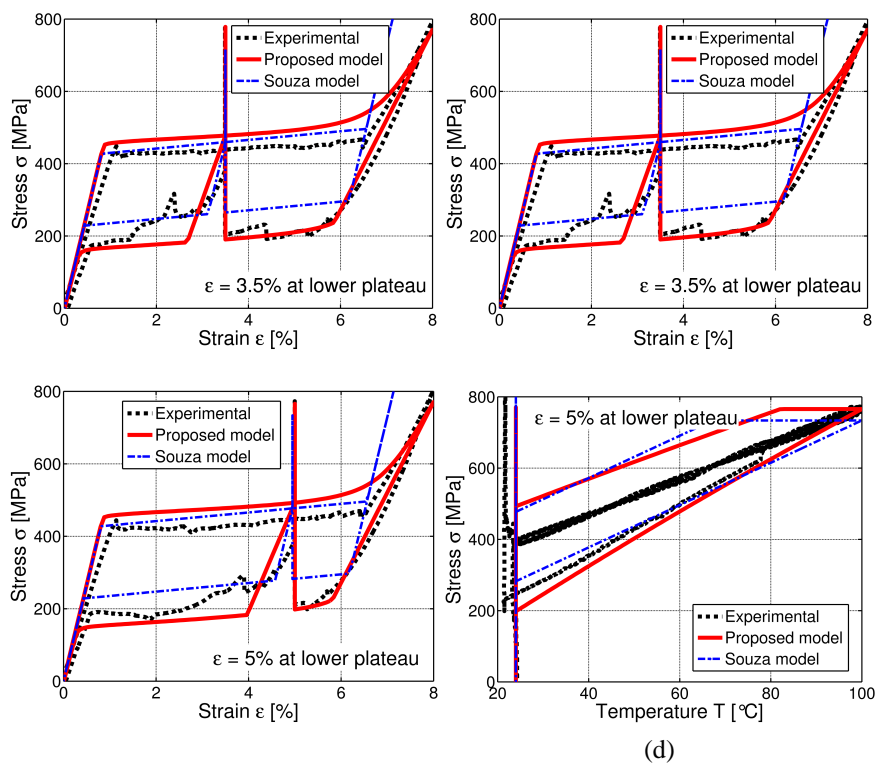


Figure 9: Model response for thermo-mechanical recovering stress tests at lower plateau.

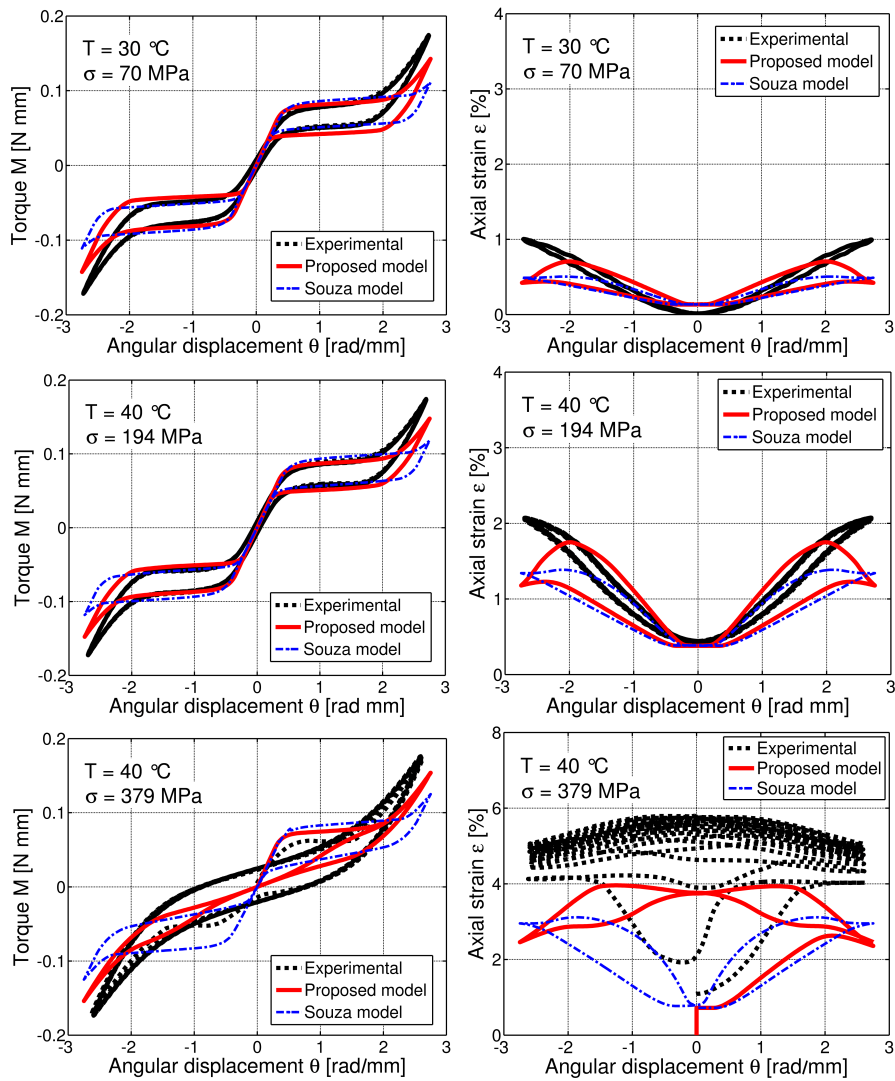


Figure 10: Model response for combined tension-torsion tests.

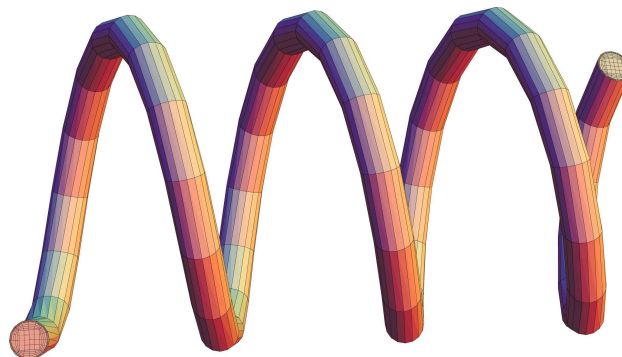


Figure 11: SMA helical spring actuator: adopted mesh.

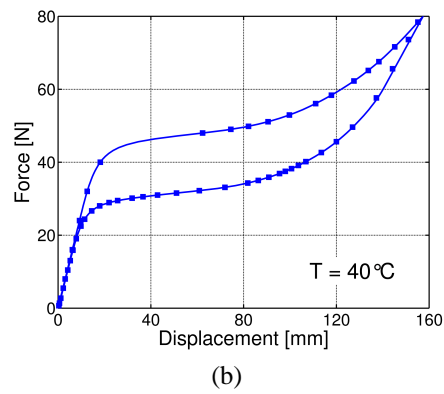
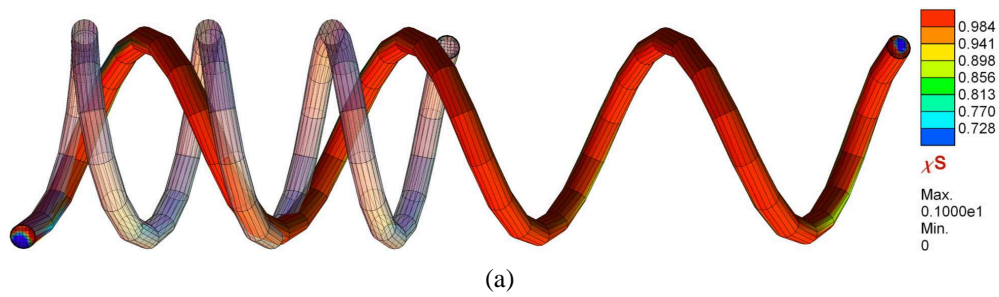


Figure 12: Pseudoelastic test of a SMA helical spring actuator: (a) spring initial geometry and scaled deformed shape under the maximum force (color map indicates distribution of the single-variant martensite volume fraction,  $\chi^S$ ); (b) force vs. vertical displacement of the loaded end of the spring diagram (markers, large load increments; solid line, small increments).

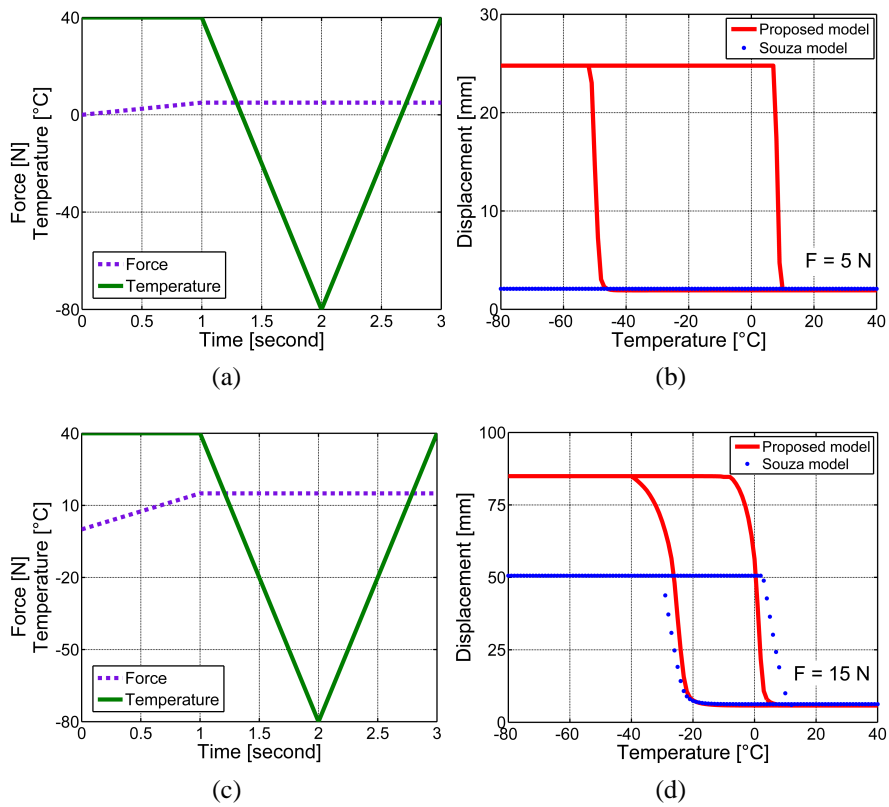


Figure 13: Thermal-cycling test at constant load of a SMA helical spring actuator: (a)-(c) temperature and force loading histories during simulation; (b)-(d) vertical displacement of the loaded end of the spring vs. temperature diagrams.